Title

A self-limiting mechanotransduction feedback loop ensures robust organ formation

Authors

Yusuke Mori[1,2], Paul Robin[3], Anne Belle Briggs[1], Daniel S. Levic[1], Jiacheng Wang[1], Kira L. Heikes[1], Michel Bagnat[1], Edouard Hannezo[3], Akankshi Munjal[1,4]

[1] Department of Cell Biology, Duke University School of Medicine, Durham, NC 27710, USA

[2] Duke Regeneration Center, Duke University School of Medicine, Durham, NC 27710, USA

[3] Institute of Science and Technology, Am Campus 1, 3400 Klosterneuburg, Austria

[4] Correspondence: akankshi.munjal@duke.edu

Abstract

Organ development requires integration of mechanical forces, biochemical signals, and transcriptional programs to achieve proper size and architecture. Mechanotransduction feedback loops convert mechanical forces into gene-expression changes that, in turn, regulate cell behaviors such as growth and extracellular matrix (ECM) production. How these loops are coupled to developmental programs to ensure robust morphogenetic outcomes remains poorly understood. Here, we show that Yap-dependent mechanotransduction establishes a self-limiting positive feedback loop that drives the successful formation of semicircular canals in zebrafish. These canals form through reproducible steps of bud initiation, extension, and fusion within the otic epithelium. Local swelling of a hyaluronan-rich ECM initiates bud formation. We demonstrate that this ECM expansion activates Yap in a spatially patterned manner within the bud. Activated Yap induces its target, *ccn1l1,* which drives further ECM production, establishing a positive feedback loop. The ensuing rapid ECM expansion sustains bud extension. Graded perturbations to the mechanotransduction loop reduced extension, with bud fusion remaining robust at lower levels of disruption but blocked at the highest dose. Critically, the loop contains its own termination mechanism: when buds fuse, the PKA-CREB signaling is activated by the adhesion GPCR Gpr126 to suppress *ccn1l1*, preventing overgrowth. These findings reveal how mechanotransduction-driven positive feedback loops can be coupled to their own termination, providing developmental control through the integration of mechanical forces with transcriptional responses and morphogenetic outcomes.

Introduction

Signaling pathways employ sophisticated feedback mechanisms to control tissue morphogenesis– the process by which tissues remodel into complex and functional organs[1,2]. Such feedback can take the form of temporal switches or self-limiting circuits, for example, the morphogen Nodal induces its own inhibitor, Lefty, to establish early embryonic patterning[3,4]. Beyond biochemical signals, developing tissues also experience and respond to physical forces. Mechanotransduction pathways sense forces such as compression, stretching, or shear and convert them into transcriptional responses that remodel the physical environment, creating feedback loops between mechanics and gene expression during morphogenesis[5,6].

Yes-associated protein 1 (Yap), a transcriptional co-activator of the Hippo pathway, is a central mechanotransducer[7]. In response to force, Yap and its co-activator Taz translocate to the nucleus, where they bind to the transcription factor Tead to activate genes that regulate proliferation, differentiation, and extracellular matrix (ECM) production[7]. By linking mechanical inputs to transcriptional programs that reshape tissue architecture, Yap provides a molecular basis for feedback between mechanics and gene expression[8]. Yet how such mechanotransduction feedback loops are spatially and temporally organized during development—and how they are ultimately terminated to avoid unchecked amplification or premature growth restriction—remains poorly understood. Understanding these principles is central to explaining how complex organ shapes emerge from the interplay of signals, forces, and transcriptional programs.

The zebrafish semicircular canals (SCC) enable addressing these questions because they allow for the simultaneous measurement of transcriptional, biochemical, and mechanical dynamics during morphogenesi[9]. SCCs arise from the otic vesicle (OV) epithelium through three discrete steps: bud initiation, extension, and fusion. Bud initiation is driven by localized synthesis of a hyaluronan- and Versican-rich ECM that osmotically swells to push the overlying epithelium[9,10]. A key challenge is to understand how this process, initiated in a small group of cells, achieves the systems-level coordination necessary to ensure the buds extend to the right size and fuse successfully. We

hypothesized that mechanotransduction could provide this coordinating mechanism, linking local ECM expansion to transcriptional responses.

Our work reveals that SCC morphogenesis is driven by a self-limiting positive feedback loop operating through Yap. Using a combination of quantitative imaging, theoretical modeling, and a live knock-in reporter of endogenous Yap, we observe that ECM expansion mechanically activates Yap in a spatially patterned manner, with peak activity at the bud border, recruiting these cells into the growing bud. Yap in turn induces *cellular communication network factor 1-like 1* (*ccn1l1,* also known as *cyr61l1*), a matricellular protein that promotes HA and Versican synthesis, ensuing rapid ECM expansion. Progressive loss of the Yap-Ccn1l1-ECM loop led to a dose-dependent reduction in extension rates, yet fusion remained robust at lower levels of disruption and was abolished only at the highest dose.

Termination of this loop occurs during bud fusion when *ccn1l1* expression declines. Analysis of mutants in a conserved adhesion GPCR, *gpr126*, previously shown to block bud fusion, revealed that *ccn1l1* expression persists, resulting in uncontrolled growth. Mechanistically, bud fusion activates the transcription factor CREB via the Gpr126-cAMP-PKA pathway, which suppresses *ccn1l1*. Thus, the morphological outcome of positive feedback–bud fusion–serves as a stop signal that terminates the very process it drives–bud extension.

Results

ECM swelling-mediated Yap activation is required for bud extension

The SCC in zebrafish develops through the remodeling of the lumenized single-layered embryonic inner ear epithelium, the basement membrane (BM)-enclosed OV, at six "canal-genesis zones" (Fig. 1a)[9,11]. Morphogenesis begins at 45 hours post fertilization (hpf) with the initiation of buds at antero-lateral, postero-lateral, and anterior zones, where cells extend into the lumen with reduced BM contact[9,12]. By 50 hpf, these buds extend, and a posterior bud begins to form. By 60 hpf, antero-lateral and anterior buds fuse, while postero-lateral and posterior buds extend, and ventral and ventro-lateral budding begins.

92 By 72 hpf, all bud pairs fuse to form the anterior, posterior, and ventral pillars, which
93 demarcate the three semicircular canals. We focused our analysis on the anterior buds,
94 which provide a clear example of all morphogenetic steps: prebudding (40 hpf), initiation
95 (45-48 hpf), extension (48-55 hpf), and fusion (55 hpf).

96 We recently demonstrated that the transcription factor Lmx1b promotes the expression
97 of *has3 (hyaluronan synthase 3)* and *vcanb (versican b),* which encode enzymes for HA
98 and Versican synthesis, respectively, at canal-genesis zones[10]. HA polymers and the
99 proteoglycan Versican that binds HA are secreted basally into the ECM, and osmotic
100 swelling of this HA-rich ECM generates pressure that pushes the overlying epithelium into
101 buds[10]. Longitudinal bud extension is maintained by tangentially distributed actomyosin
102 tethers, known as cytocinches[9]. Because ECM swelling imposes mechanical stress on
103 budding cells[9] (Extended Fig. 1a-c), we asked whether this stress engages the Yap
104 mechanotransduction pathway.

105 To characterize the dynamic localization of endogenous Yap protein *in vivo*, we
106 established a *TgKI(Yap1-mScarlet)* reporter line using a knock-in tagging method[13] (Fig.
107 1b-b'). Yap activity was quantified by calculating the nuclear-cytoplasmic ratio in budding
108 cells in embryos co-injected with H2B-GFP mRNA to visualize the nuclei. Prior to budding
109 (40 hpf), Yap was inactive, with a nuclear-cytoplasmic ratio around 1. During anterior bud
110 extension at 50 hpf, the ratio increased above 1, indicating active Yap (Fig 1c). We also
111 observed a few cells in the dorsal non-budding region of the OV with a nuclear-
112 cytoplasmic ratio greater than 1 at various stages of canal morphogenesis (Fig. 1b and
113 Extended Fig. 1d).

114 To test whether ECM-generated mechanical forces activate Yap in budding cells, we
115 injected hyaluronidase (HAase), an enzyme that degrades HA polymers, into the region
116 surrounding the OV (periotic space). As previously reported, HAase treatment caused
117 shrinkage of the bud-ECM, reduced cell stretching, and inhibited bud extension[9,14]
118 (Extended Fig. 1e-h). Significantly, nuclear localization of Yap was decreased in HAase-
119 treated embryos, with the nuclear-cytoplasmic ratio less than 1 (Fig. 1d-e). HAase
120 treatment had no effect on the nuclear-cytoplasmic ratio of non-budding cells in the dorsal

121 OV (Extended Fig. 1i). These findings were further confirmed by Yap immunostaining
122 experiments, in which the nuclear-cytoplasmic ratio in budding cells was greater than 1
123 in controls but reduced to around 1 in HAase-treated embryos (Extended Fig. 1j-m).
124 Together, these results demonstrate that Yap activation in budding cells is induced by
125 hyaluronate pressure during bud extension.

126 To examine the functional role of Yap, we performed knockdown of *yap1* using a
127 previously characterized morpholino (MO)[15]. Notably, *yap1* knockdown significantly
128 inhibited bud elongation (Fig. 1f-g), resulting in shorter lateral, anterior, and posterior buds
129 at 50 hpf. By 72 hpf, all buds had formed, but not all had fused into pillars, indicating a
130 delay in morphogenesis (Extended Fig. 1n). These data demonstrate that Yap drives bud
131 extension. To uncover the molecular mechanisms underlying this effect, we next
132 examined Yap's downstream transcriptional targets.

133 **Yap-target *ccn1l1* expression is Yap-independent at initiation and Yap-dependent**
134 **during bud extension**

135 To identify downstream targets of Yap, we used available single-cell transcriptomic
136 atlases[16-18]. A zebrafish inner-ear-specific atlas noted expression of a candidate gene,
137 *ccn1l1*, in the SCC-forming cell cluster of the OV, and this expression pattern was
138 validated at the canal-genesis zone during pre-budding and bud extension stages[16]. A
139 similar enrichment was observed in the embryo-wide Daniocell atlas[17,18], where
140 annotation of canal-forming cells using *vcanb* (Versican core protein) revealed *ccn1l1*
141 among the top 10 differentially expressed genes (Fig. 2a–b, Extended Fig. 2a). Ccn1l1 is
142 a paralog of Ccn1 and a member of the CCN family of matricellular proteins[19–21], which
143 are known downstream targets of Yap[22–25]. Importantly, the 5' upstream region of *ccn1l1*
144 contains three conserved TEAD-binding motifs recognized by Yap/Taz
145 (GGAATG/CATTCC)[22,26–28] (Extended Fig. 2b).

146 To quantitatively analyze *ccn1l1* expression dynamics at various developmental stages,
147 we used multiplexed hybridization chain reaction (HCR) fluorescence *in situ* hybridization
148 (FISH)[29]. Consistent with the single-cell atlases[16,18], *ccn1l1* expression was restricted to

149 the canal-genesis zones (Fig. 2c-d), and was detectable before bud formation at 40 hpf.
150 Its expression increased significantly during bud extension at 50 hpf, and was
151 subsequently downregulated to background levels upon bud fusion at 60 hpf (Fig. 2e).
152 Importantly, MO-mediated *yap1* knockdown led to a 50% reduction in *ccn1l1* expression
153 during bud extension (Fig. 2f-g), making it comparable to levels at the pre-budding stage,
154 confirming that *ccn1l1* is a Yap target. In contrast, *yap1* knockdown did not affect the
155 onset of *ccn1l1* expression at the pre-budding stage (Extended Fig. 2c-d). These findings
156 demonstrate that Yap is essential for increasing *ccn1l1* expression during bud extension,
157 but not for its initial onset.

158 To understand the initial regulation of *ccn1l1*, we examined its relationship with *lmx1bb*,
159 the transcription factor that, together with its paralog *lmx1ba,* we previously demonstrated
160 patterns HA and Versican synthesis during the pre-budding stage[10]. In the *lmx1bb* null
161 mutants (*lmx1b* $^{jj410/jj410}$)[29], which carry a premature stop codon, we observed a 30.1%
162 reduction of *ccn1l1* expression at the pre-budding zone compared to sibling controls
163 (Extended Fig. 2e-f). Pharmacological inhibition of Notch signaling with RO4929097,
164 which expands *lmx1bb* expression[10], similarly expanded *ccn1l1* expression compared to
165 controls (Extended Fig. 2g).

166 Altogether, these findings reveal a two-stage regulatory mechanism: Lmx1bb in part
167 initiates *ccn1l1* expression during pre-budding, while Yap amplifies *ccn1l1* expression
168 during extension. Given that Yap sustains bud extension, we hypothesized that *ccn1l1*
169 might promote the synthesis of HA and Versican, which drive bud extension. We next
170 investigated the function of *ccn1l1* to test this possibility.

171 **Ccn1l1 promotes HA and Versican synthesis to create a positive feedback loop**

172 To investigate the function of *ccn1l1*, we performed CRISPR-Cas9 or MO-mediated
173 *ccn1l1* knockdown. Consistent with its pre-budding expression pattern, the knockdown of
174 *ccn1l1* blocked the onset of budding, resulting in an absence of buds at 50 hpf and no
175 SCC at 72 hpf (Fig. 3a-b). We next asked how Ccn1l1 drives epithelial budding. CCN
176 proteins regulate cell behaviors such as adhesion, proliferation, and ECM production

177 through their conserved domains[30–32]. Zebrafish Ccn1l1 exhibits high similarity to human
178 CCN1, supporting a conserved function (Extended Fig. 3a-b). We then hypothesized that
179 bud formation failure in *ccn1l1* knockdown embryos results from loss of HA and Versican
180 synthesis. Consistent with this, *has3* and *vcanb* colocalized with *ccn1l1* at canal-genesis
181 zones (Extended Fig. 3c) and exhibited nearly identical temporal expression patterns—
182 both showing low expression during bud initiation, peaking during bud extension, and
183 returning to baseline during bud fusion, as previously reported[9,10,14] (Extended Fig. 3d).
184 Indeed, *ccn1l1* knockdown reduced *has3* and *vcanb* expression to background levels at
185 the pre-budding stage and by 50.1% and 73.5%, respectively, at bud extension (Fig. 3c-
186 d and Extended Fig. 3e-f). We conclude that Ccn1l1 drives bud initiation and extension
187 by promoting *has3* and *vcanb* transcription.

188 Given the HA-rich bud-ECM's role in Yap activation and *ccn1l1*'s role in HA production,
189 we hypothesized the existence of a positive feedback loop: *ccn1l1* expression triggers HA
190 production, generating ECM pressure that activates Yap, which in turn enhances *ccn1l1*
191 expression. This predicts that disrupting any component of this loop will affect the others.
192 First, we tested whether disrupting the mechanical force from ECM expansion would
193 affect gene expression. Consistent with our prediction, HAase treatment during bud
194 extension suppressed *ccn1l1* expression to pre-budding levels (Fig. 3e-f) and similarly
195 reduced *has3* expression (Fig. 3g-h). Second, we disrupted transcriptional regulation
196 using a heat-shock inducible dominant-negative (DN) Yap mutant lacking the TEAD-
197 binding domain[33], preventing the conversion of mechanical cues into transcriptional
198 outputs. These mutants showed significantly reduced bud extension and bud-ECM
199 volume (Fig. 3i-k), confirming that Yap's transcriptional activity is required for sustained
200 ECM production and morphogenesis.

201 Together, these complementary approaches—disrupting the mechanical arm with HAase
202 and blocking the transcriptional arm with dominant-negative Yap—demonstrate a positive
203 feedback loop where Ccn1l1 promotes ECM synthesis, ECM expansion activates Yap,
204 and Yap enhances *ccn1l1* expression (Fig. 3l). This creates a self-amplifying system that
205 can drive ECM expansion and bud extension from initially small signals. We next
206 examined how this feedback loop is spatially patterned.

207 **Mechanical patterning of cells at the bud border sustains extension for timely bud**
208 **fusion**

209 While cell proliferation and convergence-extension through cell rearrangement are typical
210 behaviors underlying tissue growth during development, our previous study showed that
211 neither is necessary for bud extension[9]. To determine the source of cells contributing to
212 this process, we performed time-lapse imaging and cell tracking. We observed a linear
213 increase in bud cell number (Fig. 4a), driven by bud-adjacent cells moving toward the
214 initiated bud, turning at its border, and becoming incorporated into the extending structure
215 (Fig. 4b). Disruption of ECM expansion with HAase treatment or mechanotransduction
216 with *yap1* MO inhibited this increase in cell number (Fig. 4c-d). This suggests that ECM-
217 expansion through mechanotransduction exerts pulling forces that recruit adjacent cells
218 into the growing bud.

219 Because recruitment occurs specifically at the bud border, we hypothesized that
220 mechanotransduction cues are spatially patterned rather than uniform. To explore this,
221 we developed a theoretical vertex model of a 2D epithelial section incorporating
222 experimentally established parameters[9]: apical, lateral, and basal cellular tension; BM
223 adhesion at the bud border; HA-rich bud-ECM pressure; and anisotropic cytocinch
224 tension orthogonal to the bud's long axis (Fig. 4e and Extended Fig. 4a-d; see
225 Supplementary Note). The model defines four mechanically distinct regions: bud-adjacent
226 cells (BM-attached), bud border cells (partially BM-attached), budding cells (newly
227 incorporated, BM-detached), and tip cells (leading-edge, BM-detached) (Fig. 4e).

228 The model indicated that cell recruitment was accompanied by a transient increase in cell
229 aspect ratio (Fig. 4f), with stronger overshoots in border and budding cells compared to
230 tip cells. This spatial pattern was lost when BM attachment or cytocinches were removed
231 (Extended Fig. 4a-d), suggesting that mechanical stress is concentrated at the border
232 cells attached to the BM. To test this, we measured nuclear aspect ratios as a marker of
233 cell deformation[34,35] and found that border cells were indeed more deformed than tip cells
234 (Fig. 4g). Supporting the higher mechanical stress prediction, the Yap reporter showed
235 higher activity in border and budding cells, with notably lower variability in border cells

236 indicating Yap activation during recruitment (Fig. 2b-b' and Fig. 4h). Notably, *ccn1l1*
237 expression was slightly lower in border cells than in budding cells, consistent with recent
238 Yap activation (Fig. 2d). Together, these results demonstrate that Yap activity is spatially
239 patterned at the bud borders rather than occurring throughout the bud. Consistent with
240 this,

241 To test the functional significance of spatially patterned mechanotransduction, we
242 modeled bud growth dynamics in which ECM production comprised two components: a
243 constant baseline rate from pre-patterned tip cells and a mechanotransductive
244 contribution proportional to the number of recruited cells. When mechanotransduction
245 strength is high, the model predicts accelerated, non-linear ECM volume growth (Fig. 4i).
246 In contrast, disabling the mechanotransductive contribution, resulted in a slower, more
247 linear increase in ECM volume consistent with constant ECM production from tip cells
248 alone (Fig. 4i). Because bud extension in the model depends on ECM volume growth,
249 reduced ECM production without mechanotransductive contribution led to slower
250 extension rates (Fig. 4k). As predicted by the model, control embryos exhibited rapid ECM
251 growth and faster extension compared to *yap1* MO-injected embryos that showed slower
252 ECM growth and reduced bud extension (Fig. 4j and 4l).

253 Extending buds eventually meet and fuse to form pillars, completing otic vesicle
254 remodeling and canal demarcation. We next examined how varying extension rates, set
255 by ECM produced by tip cells and by the mechanotransductive recruitment of neighboring
256 cells, determine whether buds achieve fusion. To address this, we generated a phase
257 diagram from ~500 simulations varying both parameters, with fusion defined as buds
258 reaching 30 μm in length (Fig. 4m), which corresponds to the average distance required
259 for opposing buds to make contact across the otic vesicle lumen in wild-type embryos at
260 60 hpf (Extended Fig. 5a). The simulations revealed a trade-off: when
261 mechanotransduction strength is low, fusion was delayed and required high tip cell
262 contribution, whereas with high mechanotransduction, even minimal tip cell production
263 was sufficient for bud fusion (Fig. 4m and Extended Fig. 4e). To test these predictions
264 experimentally, we performed dose-dependent MO-knockdowns of *ccn1l1* (Fig. 4n-o and
265 Extended Fig. 4f), which affects both tip cell and mechanotransductive ECM production.

266 At lower doses, extension slowed significantly, but buds still fused successfully by 72 hpf
267 (Fig. 4n-o). At the highest dose, extension dropped below ~95% of normal rates (Fig. 4n)
268 and buds failed to fuse (Fig. 4o). Thus, mechanotransduction ensures that buds can still
269 achieve fusion across a wide range of tip cell output, with failure occurring only under the
270 most severe loss of ECM production.

271 Our theoretical model and experimental data demonstrate that mechanical deformation
272 at bud borders activates Yap to drive cell recruitment and ECM expansion, sustaining bud
273 extension rates that ensure successful fusion even when tip cell ECM production varies.

274 **CREB activation during fusion terminates the positive feedback loop**

275 Intriguingly, *ccn1l1* expression dropped sharply once opposing buds fused (Fig. 2c and
276 2e). Consistent with this downregulation, both cell recruitment and bud extension
277 plateaued when bud pairs made contact (Fig. 4a and Extended Fig. 5a), indicating a self-
278 termination mechanism that stops further bud growth. A likely candidate for this stop
279 signal is Gpr126 (Adgrg6), a mechanosensitive adhesion-type G-protein-coupled
280 receptor (aGPCR) essential for bud fusion[14,36,37] and expressed in budding cells
281 throughout morphogenesis[14] (Extended Fig. 5b). Consistent with previous findings[14], in
282 *gpr126*$^{st49/st49}$ mutants, which carry a premature stop codon[38], buds fail to fuse and
283 undergo excessive elongation, accompanied by persistent *has3* expression (Fig. 5a-c and
284 Extended Movie 2-3). We found that *ccn1l1* expression remained persistently elevated in
285 these mutants at both 60 hpf and 72 hpf, contrasting with the normal sharp
286 downregulation upon fusion (Fig. 5b-c and Extended Fig. 5c) . This persistent expression
287 drove continued growth: mutant buds were 78.7% longer and contained 76.5% more cells
288 than wild type at 60 hpf (Fig. 5d-e). Notably, bud-ECM volume continued to grow
289 unchecked, with a 464.6% increase in volume (Fig. 5f and Extended Fig. 5d), consistent
290 with the ongoing recruitment of HA-producing cells. This behavior is inconsistent with a
291 genetically predetermined bud cell number, which would have produced a plateau in
292 extension. Instead, this provides further evidence that mechanotransduction recruits new
293 cells to the bud. The 2D vertex model recapitulated this behavior: when fusion was
294 blocked and the mechanotransductive contribution proportional to recruited cells allowed

295 to persist, ECM volume expanded unchecked (Extended Fig. 5e). These results
296 demonstrate that bud fusion provides the essential termination signal for the positive
297 feedback loop; in its absence, mechanotransductive recruitment drives runaway growth.

298 We next investigated how Gpr126 terminates *ccn1l1* expression. Gpr126 activates the
299 cyclic adenosine monophosphate (cAMP) pathway[39,40]. Pharmacological cAMP elevation
300 with forskolin[41] strongly reduced both *ccn1l1* and *has3* expression (Extended Fig. 5f-g)
301 and inhibited bud elongation (Extended Fig. 5h-i). Since cAMP signals via Protein Kinase
302 A (PKA), leading to the phosphorylation of the transcription factor CREB[42], we examined
303 CREB activation during fusion. Immunostaining revealed striking CREB phosphorylation
304 at bud-bud contact sites, spreading into budding cells that form the pillar (Fig. 5g). This
305 CREB phosphorylation was absent in *gpr126* mutants (Fig. 5h), demonstrating that
306 Gpr126 signaling mediates the phosphorylation of CREB.

307 CREB has been reported to downregulate CCN gene transcription in cultured cells[43,44].
308 To confirm the role of CREB in the inhibition of *ccn1l1*, we expressed DN-PKA lacking the
309 cAMP-binding site[45]. This attenuated CREB phosphorylation and prevented both bud
310 fusion and *ccn1l1* downregulation (Fig. 5i-j and Extended Fig. 5j-k), demonstrating that
311 PKA-CREB signaling is necessary for feedback termination.

312 Together, these results demonstrate that the Gpr126-cAMP-PKA-CREB pathway
313 suppresses *ccn1l1* and terminates ECM synthesis during bud fusion. This creates a
314 morphological transition-triggered, self-limiting mechanism where the successful
315 completion of morphogenesis (fusion) terminates the positive feedback loop.

316 **Discussion**

317 Our findings reveal how robust SCC morphogenesis emerges from a self-limiting positive
318 feedback mechanism where morphological success triggers its own termination. We
319 demonstrate that the mechanotransducer Yap, activated by a HA-rich ECM, drives the
320 expression of the matricellular protein Ccn1l1, which further promotes HA and Versican
321 synthesis to sustain ECM expansion and bud extension. This positive feedback loop is
322 spatially restricted, with Yap activity highest at the bud border. Critically, the Gpr126-

323 cAMP-PKA-CREB pathway is activated during bud fusion and terminates *ccn1l1*
324 expression, preventing runaway growth. Thus, the completion of morphogenesis serves
325 as the signal to terminate the very process that drives it.

326 Most studies of Yap/Taz mechanotransduction have emphasized their role in negative
327 feedback loops that maintain tissue homeostasis, where mechanical forces activate
328 Yap/Taz to promote behaviors that ultimately dissipate those same forces[26,46–48]. More
329 recently, however, it has become clear that Yap/Taz can also participate in positive
330 feedback loops[49] to amplify mechanical cues rather than inhibiting them. Here we show
331 that Yap activation promotes ECM synthesis, which generates mechanical forces that
332 further sustain Yap activtity to generate self-reinforcing growth dynamics. We propose
333 that this positive feedback mechanism may be important during developmental windows
334 where weak initial signals must be robustly amplified to drive rapid morphogenetic
335 outcomes.

336 The identification of Ccn1l1 as a key mediator linking Yap activation to ECM production
337 represents a significant advance in understanding how CCN proteins contribute to
338 mechanotransduction networks. While CCN family proteins have been implicated in
339 developmental processes, wound healing, and inflammation[19–21], their specific role in
340 creating positive feedback loops between mechanical forces and matrix synthesis has not
341 been previously demonstrated. The two-stage regulation of Ccn1l1—initial Lmx1b-
342 dependent expression followed by Yap-dependent amplification—suggests an elegant
343 mechanism for transitioning from developmental patterning to mechanically-driven growth
344 amplification. Notably, *ccn1l1* is also expressed in other organs, including somite and
345 notochord[19], raising the possibility that similar feedback-driven mechanisms operate more
346 broadly during vertebrate development.

347 CCN proteins are known to interact with integrins to regulate ECM production[30–32], and
348 among them, β1 integrin is a well-documented receptor for CCN family members[24,31,50].
349 β1 integrin expression has indeed been reported in the OV of both zebrafish and mice[51,52],
350 suggesting that *ccn1l1* may act via integrin to promote ECM production during SCC
351 formation. Beyond ECM regulation, CCN proteins can also remodel the actomyosin

352 cytoskeleton through integrin-Rho GTPase signaling, thereby promoting cellular
353 protrusions and generating mechanical tension[24]. We previously reported that
354 cytocinches progressively increase during bud extension and are essential for longitudinal
355 growth[9], coinciding with the rise in *ccn1l1* expression. These observations raise the
356 possibility that *ccn1l1* not only promotes ECM expansion, but may also contribute to bud
357 extension by modulating cytoskeletal tension.

358 Our theoretical model predicts that BM attachment is crucial for spatially restricting Yap
359 activation to border cells, yet this prediction remains to be investigated. Integrins,
360 particularly those that bind laminin components of the BM[53], are prime candidates for
361 transducing mechanical forces at these sites. Focal adhesion kinase (FAK) and related
362 signaling molecules, such as vinculin, likely serve as mechanosensitive intermediates that
363 link integrin engagement to Yap activation[7]. The precise mechanical threshold required
364 for Yap activation, and how BM composition and stiffness modulate this threshold,
365 represents an important avenue for future investigation. Understanding these molecular
366 details could reveal how tissues fine-tune their mechanosensitivity during morphogenesis.

367 Adhesion GPCRs (aGPCRs) perform diverse developmental roles in many organs like
368 heart, sciatic nerve, cartilage, and vascular systems, and their dysfunction can lead to
369 organ malformation or embryonic lethality[36,54–57]. Previous work implicated Gpr126 in
370 downregulating ECM production during SCC formation[14], but the molecular mechanism
371 was unknown. We find that Gpr126 signaling is activated during fusion and terminates
372 ECM production by downregulating *ccn1l1*. Such termination mechanisms may represent
373 a conserved principle by which aGPCRs couple tissue remodeling to signaling and
374 transcriptional outcomes during morphogenesis. Although the precise mode of Gpr126
375 activation remains unclear, it likely involves ligand binding and/or mechanical forces that
376 expose a tethered agonist (Stachel sequence) to trigger downstream signaling[58–61].

377 The integration of mechanotransduction feedback loops to morphological outcomes
378 provides a framework for understanding how complex organ shapes emerge through self-
379 organizing principles. Overall, we demonstrate how robust SCC morphogenesis emerges
380 from an interplay of two evolutionarily conserved pathways. The mechano-transduction

381 feedback loop, Yap-Ccn1l1-HA, drives bud extension, and the Gpr126-cAMP-PKA-CREB
382 pathway couples bud fusion to extension termination. This principle likely applies broadly
383 to developmental systems where patterned growth-promoting signals must first be
384 amplified and then precisely shut down.

385 **Materials and Methods**

386 **Animals**

387 Zebrafish (*Danio rerio*) EK and AB wild-type strains were used in this study. Adult fish
388 were kept on a 14-hour light/10-hour dark cycle. Embryos were collected by crossing
389 female and male adults (3-18 months old) and raised in 28.5 °C egg water. In this study,
390 the following transgenic and mutant lines were used: *Tg(actb2:membrane-neongreen-*
391 *neongreen)*[9], *lmx1bb*$^{jj410/jj410}$ [38], *Tg(hsp70l: RFP-DN-Yap1)* (this study), *Tg(hsp70l: DN-*
392 *PKA-GFP)* (this study), *gpr126* $^{st49/st49}$ [38], *TgKI(Yap1-mScarlet)* ^{pd1280} (this study), and
393 *Tg(βActin: utrophin-mCherry)*[62]. *gpr126* $^{st49/st49}$ mutant fish were maintained as an AB
394 strain background, whereas all other transgenic and mutant lines were maintained as an
395 EK strain background.

396 **Morpholino injection**

397 Standard control MOs and MOs targeting *ccn1l1* (5′-
398 CTCAGAGGAGACATGGTGTTATCCA-3′, translational blocking), *yap1* (5′-
399 AGCAACATTAACAACTCACTTTAGG-3′, splice-modifying between intron 2 and exon 2)
400 [15], and *p53* (5′-GCGCCATTGCTTTGCAAGAATTG-3′, translational blocking)[63] were
401 purchased from Gene Tools. The *ccn1l1* MO *target sequence* was designed based on
402 the Danio rerio *ccn1l1* mRNA sequence (ENSDART00000051336), retrieved from the
403 Ensembl database, using the Gene Tools Oligo design service. For the *ccn1l1* knockdown,
404 embryos at the single-cell stage were injected with 2 ng of *ccn1l1* MO or control MO,
405 together with 1 ng of *p53* MO. For the *yap1* knockdown, 5 ng of *yap1* MO was injected
406 with 2.5 ng of *p53* MO into embryos at the single-cell stage. MO-injected embryos were
407 screened for inner ear phenotype at 40-50 hpf and used for confocal live imaging, HCR-
408 FISH, or immunostaining at 40-72 hpf. To test the dose-dependent effect of *ccn1l1* MO,

409 embryos at the single-cell stage were injected with either standard control MO (2 ng) or
410 *ccn1l1* MO (0.5, 1, or 2 ng), together with *p53* MO. Injected embryos were screened for
411 inner ear phenotype at 50 hpf, followed by confocal live imaging at 50, 56, and 72 hpf.
412 *p53* MO was co-injected with control, *ccn1l1* or *yap1* MO to reduce MO-injection induced
413 apoptosis and non-specific toxity.

414 **Genome editing by CRISPR-Cas9**

415 *ccn1l1* CRISPANT embryo

416 Single-guide RNAs (sgRNAs) were synthesized as previously reported[10]. Briefly, sgRNAs
417 targeting multiple coding regions of *ccn1l1* were synthesized using MEGAscript SP6
418 Transcription Kit (Invitrogen, AM1330) and purified with RNA Clean & Concentrator kit
419 (Zymo Research, R1018). For the knockdown of *ccn1l1*, three sgRNAs were pooled
420 together and injected into embryos as previously described[10]. Briefly, embryos at the
421 single-cell stage were injected with 2 nL of injection solution containing pooled sgRNAs
422 (200 ng/μL: 66.6 ng/μL of each sgRNA) and Cas9 protein (PNA Bio, CP-03, 500 ng/μL).
423 F0 crispant embryos were screened for inner ear phenotype at 50-72 hpf and then used
424 for HCR-FISH or confocal live imaging. The following target sites were used to generate
425 sgRNAs: *ccn1l1* sgRNA1: 5'-CGGCGGGCACAGCGCCAGTCGGG-3'; *ccn1l1* sgRNA2:
426 5'-GTGTGTCCTCAGGTGCAGGGAGG-3'; *ccn1l1* sgRNA3: 5'-
427 AGGTGGCTGGAGCGATAGGGCGG-3'

428 *tyrosinase* CRISPANT embryo

429 A sgRNA targeting the *tyrosinase* gene[64] was synthesized as described above. sgRNA
430 (200 ng/μL) and Cas9 protein (500 ng/μL) were injected into embryos at the one-cell stage
431 as described above. The *tyrosinase* crispant embryos were screened for pigmentation
432 loss at 50-72 hpf and used for HCR-FISH or confocal live imaging. *tyrosinase* crispant
433 embryos were used as an sgRNA injection control, resulting in loss of pigmentation
434 without affecting SCC formation[10]. The following target site was used to generate the
435 sgRNA: 5′-GGACTGGAGGACTTCTGGGG-3′.

436 Generation of *TgKI(Yap1-mScarlet)* line

437 The *TgKI(Yap1-mScarlet)* ^{pd1280} line was generated using a previously reported knock-in
438 tagging method[13]. As the targeting cassette, a gene fragment spanning from the middle
439 of intron 7 to the last codon of exon 8 was cloned into pUC19-TgKI-MCS-mScarlet-MCS-
440 polyA (Addgene plasmid #174023) using In-Fusion seamless cloning (Takara Bio) with
441 the following primers: *yap1* Fw: 5′-
442 TTCGCTAGCCCGCGGCTATCAGTGCTTTACAGATCATTGTC-3′; *yap1* Rev: 5′-
443 CACCTCGAGTCTAGATAGCCAGGTTAGAAAGTTCTCC-3′. The sgRNA target sites for
444 genomic editing were mutated in the donor plasmid using Q5 site-directed mutagenesis
445 (New England Biolabs, NEB) with the following primers: *yap1* SDM Fw: 5′-
446 ACATCCTCAACGACATGGAGTCAGTGCTGGC-3′; *yap1* SDM Rev: 5′-
447 CGGAGCTCAAAGCTTCCTGCAGGCTGGGCA-3′. A sgRNA targeting *yap1* (5′-
448 GTTGAGGATGTCGGAGCTTAGGG-3′) was synthesized using the HiScribe T7 Quick
449 High Yield RNA Synthesis Kit (NEB) and purified with the Monarch RNA Cleanup Kit
450 (NEB). The injection mix contained PCR donor (20 nM), gRNA (4 μM), Cas9 protein (3
451 μM; PNA Bio CP-02), and DMSO (1%). The genomic integration site was confirmed by
452 sequencing at the F2 generation, and the line was designated allele number pd1280.

453 **Construct the generation and injection of plasmid and mRNA**

454 *actb2:H2B-EGFP* plasmid

455 H2B-EGFP was amplified by PCR using Phusion Flash High-Fidelity PCR Master Mix
456 (Thermo Fisher Scientific, F548L) and appropriate primers from a construct harboring its
457 coding sequence. pMTB *actb2:membrane-neongreen-neongreen* construct[9], which
458 contains the SP6 promoter for mRNA synthesis, was used as the plasmid backbone. The
459 plasmid backbone was digested with BamHI and AgeI. Then, the amplified H2B-EGFP
460 fragment was cloned downstream of the actb2 promoter and the SP6 promoter in the
461 pMTB backbone using In-Fusion Snap Assembly Master Mix (Takara, 638948). The H2B-
462 EGFP mRNA was synthesized using the mMESSAGE mMACHINE SP6 transcription kit
463 (Invitrogen, AM1340) from the linearized *actb2:H2B-EGFP* plasmid. 2nL of mRNA (100

464 ng/μL) was injected into single-cell-stage embryos from *TgKI(Yap1-mScarlet)* parents.
465 Live embryos were observed at 40-56 hpf by confocal microscopy. The following primers
466 were used for PCR: Fw: 5'-
467 CTTGTTCTTTTTGCAGGATCCCGCCACCATGCCAGAGCCAGCGA-3'; Rev: 5'-
468 TTATCATGTCTGGATCACCGGTTTACTTGTACAGCTCGTCCATGC-3'.

469 *hsp70l: RFP-dominant negative Yap1* plasmid

470 hsp70l: RFP-DN-Yap1[33] construct harboring the I-Sce Ⅰ site for the transgene was a gift
471 from Kenneth Poss (Morgridge Institute, University of Wisconsin-Madison, USA) and was
472 used as a template for cloning. RFP-DN-Yap1 was amplified by PCR using appropriate
473 primers. The plasmid backbone, which contains a heat-shock-inducible promoter (hsp70l)
474 and Tol2 sites, was digested with BamH1 and AgeI and then gel-purified. The amplified
475 DNA fragment was cloned downstream of the hsp70l promoter in the plasmid backbone
476 using the In-Fusion system. To generate the *Tg(hsp70l: RFP-DN-Yap1)* line, 100 pg of
477 Tol2 mRNA and 50 pg of hsp70l: RFP-dnYap1 plasmid were injected into embryos at the
478 one-cell stage. The following primers were used for PCR: Fw: 5'-
479 TTGCAGGATCCGCCACCATGGACAACACCGAGGACG-3'; Rev: 5'-
480 TGGATCACCGGTTCAGATACTACTGTGGGCTGGAGGG-3'

481 *hsp70l: dominant negative PKA-GFP* plasmid

482 M7 pdnPKA-GFP was a gift from Randall Moon (Addgene plasmid # 16716), used as a
483 template for cloning. The cloning was performed, as described above. Briefly, the
484 amplified dnPKA-GFP fragment was cloned downstream of the hsp70l promoter in the
485 plasmid backbone. To generate the *Tg(hsp70l: DN-PKA-GFP)* line, 100 pg of Tol2 mRNA
486 and 50 pg of hsp70l: DN-PKA-GFP plasmid were injected into embryos at the one-cell
487 stage. The following primers were used for PCR: Fw: 5'-
488 TACAGTTCAGCCATCCTAGGATTTAGGTGACACTATAGAATACAAGCTACT-3'; Rev:
489 5'-GTTCCGGATACGTATGAATTCTTATTTGTATAGTTCATCCATGCCATGT-3'

490

491 **Drug treatment**

492 For hyaluronidase treatment, we injected hyaluronidase (HAase, Sigma Aldrich, H1136)
493 into the periotic space of dechorionated embryos, with slight modifications to a previously
494 reported method[9]. Briefly, HAase (500 units/mL) was injected into embryos twice at a 3-
495 hour interval from 46 hpf, followed by HCR-FISH or confocal live imaging. For live imaging
496 of *TgKI(Yap1-mScarlet)* embryos, HAase was injected into embryos at 50 hpf, followed
497 by imaging at 1.5 hours post-injection. For immunostaining of Yap1 antibody, HAase was
498 injected into embryos at 50 hpf, and embryos were fixed with 4% PFA in PBS at 3 hours
499 post-injection, followed by immunostaining. For RO4929097 (ApexBio, A4005) treatment,
500 dechorionated embryos at 24 hpf were soaked in egg water containing 50 μM inhibitor for
501 26 hours, followed by HCR-FISH. For forskolin (Cayman Chemical, 1101810) treatment,
502 dechorionated embryos were soaked in egg water containing 50 μM of the drug at 46 hpf
503 for 6 hours, followed by HCR-FISH or confocal live imaging.

504 **Multiplex *in situ* hybridization chain reaction (HCR)**

505 HCR probes for each gene were obtained from IDT (Oligo Pools, oPools). Hybridization
506 buffer, amplification buffer, wash buffer, and amplifiers were purchased from Molecular
507 Instruments. mRNA sequences used for HCR probe design were retrieved from the NCBI
508 database. HCR probe sets for each mRNA were designed using a home-made Python
509 script[29]. 40 probe oligonucleotides targeting each mRNA were generated and pooled
510 oligonucleotides were used for HCR-FISH. HCR probe sequences are listed in Extended
511 Table 1. HCR-FISH experiments were performed as previously described[9,10].
512 Dechorionated embryos at various stages were fixed with 4% paraformaldehyde (PFA) in
513 PBS and permeabilized with prechilled acetone. The embryos were then incubated with
514 the hybridization buffer at 37°C for 30 min, followed by incubation with the hybridization
515 solution containing probes overnight at 37°C. After probe hybridization, the embryos were
516 incubated overnight at room temperature in an amplification buffer with fluorescent HCR
517 amplifiers (Alexa-488, Alexa-546, or Alexa-647). Embryos were washed with 0.1%
518 Tween-20 in 5× SSC buffer (four times) and stored at 4°C until confocal imaging. Control
519 and experimental samples were processed within the same tube to ensure uniform

520 treatment. This included the same incubation times, reagent concentrations, and handling
521 procedures, ensuring that any differences in fluorescence intensity were due to variations
522 in target abundance rather than experimental variability.

523 **Immunohistochemistry**

524 Immunohistochemistry was performed as previously described[10]. Briefly, for phospho-
525 CREB staining, the dechorionated embryos were fixed with 4% PFA/PBS for 2 hours at
526 room temperature, followed by permeabilization with pre-chilled acetone at -20 °C for 7
527 minutes. Embryos were then blocked with 5% bovine serum albumin (BSA; Sigma-Aldrich,
528 A3311) in 1× PBS containing 0.1% Tween-20 (PBT) at room temperature for 1 h, followed
529 by incubation in primary antibody solution containing rabbit anti-phospho-CREB (Ser133)
530 antibody (Cell Signaling Technology, 9198; 1:100) and mouse anti-GFP antibody
531 (Invitrogen, A11120; 1:500) at 4°C overnight. Embryos were washed with 1x PBT for 5
532 min, thrice, then incubated with a secondary antibody solution containing fluorescently
533 labeled anti-rabbit and anti-mouse antibodies (Thermo Fisher Scientific, A11008, A11035,
534 A21244, and A11001; 1:200) and phalloidin (Thermo Fisher Scientific, A22287; 1:100) at
535 4°C overnight. Embryos were washed with 1x PBT for 5 min, thrice, and stored at 4°C.
536 For Yap1 staining, embryos fixed with 4% PFA/PBS were permeabilized with 2% Triton
537 X-100/PBS for 2 hours. Embryos were then blocked with 2% BSA in 1× PBS containing
538 1% DMSO and 0.1% Triton X-100 (PBDT) for 2 hours at room temperature, followed by
539 incubation in a primary antibody solution containing rabbit anti-Yap1 (Proteintech, 13584-
540 1-AP; 1:200) at 4 °C overnight. Embryos were washed with 1× PBDT for 15 min, thrice,
541 then incubated with a secondary antibody solution containing fluorescently labeled anti-
542 rabbit antibody (1:200) and Hoechst 33342 (Thermo Fisher Scientific, 62249; 1:2000) at
543 4°C overnight. Following this, embryos were washed with 1× PBDT for 15 minutes, thrice.

544 **Confocal imaging**

545 Confocal imaging was performed with a Zeiss LSM 980 confocal microscope using a C-
546 Apochromat 40×1.2 NA objective for all fluorescence acquisitions as previously
547 described[10]. Briefly, dechorionated live embryos were anesthetized in 1xtricaine and then

548 mounted dorsolaterally using a canyon mount cast in 1.5% agarose dissolved in egg
549 water and covered with a coverslip. Images of *TgKI(Yap1-mScarlet)* embryos were
550 acquired using Airyscan SR mode, followed by image processing using the Zen software
551 (Zeiss). For imaging of embryos stained with HCR-FISH or immunohistochemistry,
552 embryos were mounted on 1.5% agarose dissolved in 1x PBS and then subjected to
553 confocal imaging. Image acquisition settings, such as laser power, gain, and exposure,
554 were kept constant and within the sub-saturation range during microscopy to allow for
555 accurate and quantitative sample comparisons. Time-lapse imaging was performed as
556 previously described[9]. Briefly, embryos were immobilized by injecting 500 μM α-
557 bungarotoxin protein in PBS (Thermo Fisher Scientific, B35450) into the heart 30 min
558 before imaging. The embryos were maintained in a custom-built incubator at 28.5°C
559 during time-lapse imaging. Z-stack images were acquired at 30-minute intervals.
560 FluoRender, an open-source software, was used for 3D renderings of images.

561 **Screening and genotyping of mutants**

562 *gpr126* $^{st49/49}$ mutants, derived from *gpr126* $^{st49/+}$ parents, were screened for
563 immunohistochemistry based on inner ear phenotypes at 60 hpf[14]. For Fig. 5a–f and
564 Extended Fig. 5d, EK wild-type and *gpr126* $^{st49/49}$ mutants were obtained from EK wild-
565 type and *gpr126* $^{st49/49}$ parents, respectively, and subsequently subjected to HCR-FISH
566 and confocal live imaging at 50-72 hpf. To minimize developmental differences between
567 mutant and wild-type embryos, male and female fish were maintained in a mating tank
568 separated by a removable divider overnight, and fertilized eggs were collected within 15
569 minutes after the divider was removed the following morning. *lmx1bb* $^{jj410/+}$ mutants were
570 genotyped using the derived cleaved amplified polymorphic sequence (dCAPS) method,
571 as previously described[10]. The *lmx1bb* $^{jj410/jj410}$ mutant obtained from *lmx1bb* $^{jj410/+}$ parents
572 was screened based on inner ear phenotypes at 50 hpf, followed by HCR-FISH.

573 **Heat-shock activation of hsp70l promoter**

574 For experiments using DN-Yap1 mutants, *Tg(Hsp70l: RFP-DN-Yap1)* fish were crossed
575 with *Tg(actb2:membrane-neongreen-neongreen)* fish. Embryos obtained from this cross

were heat-shocked at 37°C for 30 min twice at 5-hour intervals at 40 hpf, followed by confocal live imaging at 50 hpf. DN-Yap1 mutants were identified by RFP fluorescence at 5 hours post-heat shock. RFP-negative siblings were used as controls for confocal imaging. For experiments using DN-PKA mutants, *Tg(Hsp70l: DN-PKA-GFP)* fish were crossed with wild-type or *Tg(βActin:utrophin-mCherry)* fish. To induce acute activation of the heat-shock promoter before bud fusion, embryos were heat-shocked at 42°C for 10 min at 48 hpf, followed by HCR-FISH or confocal live imaging at 56 hpf. DN-PKA mutants were identified by GFP fluorescence at 3 hours post-heat shock. GFP-negative siblings were used as controls for HCR-FISH or confocal live imaging. Heat-shock treatment at 42°C for 10 min was confirmed not to noticeably affect zebrafish embryonic development.

Modeling

See Theory Supplementary Note

Analysis of single-cell RNA sequencing data

Single-cell RNA sequencing analysis was performed using Daniocell2023_SeuratV4.rds[17,18] available at https://daniocell.nichd.nih.gov/. The published Seurat object was processed in R (v 4.4.0) using Seurat (v5.2.1)[65]. The R script of this analysis can be obtained at GitHub (https://github.com/MunjalLab/ccn1l1_project). Clusters of otic tissue cells from 36 hpf to 72 hpf were isolated from the original Daniocell atlas. 3000 highly variable genes were selected using the Seurat function 'FindVariableFeatures' with the method 'vst'. All genes were then scaled to have a mean expression of 0 and a variance of 1 across all selected cells. Clustering was performed using the Louvain algorithm[66] implemented in FindClusters with a resolution of 0.6. The canal-forming cell cluster was identified based on expression of *vcanb*, a known marker for this cell type, supported by previous literature[10,14]. The top 10 differentially expressed genes were identified by the 'FindAllMarkers' function in Seurat.

Comparative analysis of Ccn1l1 and Ccn1 amino acid sequences

602 For the analysis of the functional domains of zebrafish Ccn1l1, amino acid sequences
603 were retrieved from the NCBI database. Functional domains were predicted using the
604 SMART database[67,68], and the significance (E-value) of each predicted domain was
605 recorded. To compare domain conservation across species, multiple sequence
606 alignments were performed using Clustal Omega[69], and sequence similarity and percent
607 identity were assessed. Clustal alignment outputs were used to visualize conserved
608 residues, and the pairwise identity matrix was used to quantify percent identity between
609 species. Amino acid sequences of each functional domain predicted by SMART are listed
610 in Extended Table 2.

611 **Analysis of the TEAD-binding domain in *ccn1l1* 5' upstream region**

612 For this analysis, genomic DNA was extracted from EK wild-type embryos at 2 dpf, and
613 a 7-kb fragment of the *ccn1l1* 5′ upstream region was amplified by PCR. The sequence
614 of the PCR product was determined by Sanger sequencing and analyzed for the presence
615 of the TEAD-binding motif (GGAATG/CATTCC)[22,26–28]. The following primers were used
616 for PCR: forward, 5′- TATGTCAAACACACAAGCAGTGG-3′; reverse, 5′-
617 GGTGTTATCCAAAAAATTGTTAAGAGGC-3′.

618 **Quantification and statistical analysis**

619 **1) Bud length measurement**

620 For quantification, images were acquired by confocal live imaging of embryos expressing
621 membrane-NeonGreen, with z-stacks collected at 0.5 or 1 μm intervals. 2D images
622 capturing the middle section of the bud were used to measure the bud length of embryos.
623 Bud lengths were measured manually using the "straight-line" tool in Fiji. Where budding
624 had not started or in perturbations where budding was affected, bud lengths correspond
625 to average cell height at the anterior or posterior region. For time-lapse analysis, the same
626 buds were tracked every 30 min, and the bud length was measured at each time point.
627 For the anterior bud length of *gpr126*$^{st49/st49}$ mutants or the anterior pillar of WT embryos
628 (Fig. 5), bud length was measured by Imaris software. Using the spot tool, spots were

629 placed along the centerline of the bud, and the total length was calculated by connecting
630 these spots.

631 **2) Cell and nuclear aspect ratio**

632 The cell aspect ratio of budding cells was measured using the “straight-line” tool in Fiji. Z-
633 stack images of the OV in embryos expressing membrane-NeonGreen were obtained by
634 confocal live imaging at 0.5 μm intervals. 2D images capturing the middle section of
635 budding cells were used to measure cell height and width, as shown in Extended Fig. 1a.
636 For time-lapse analysis, the same cells were tracked every 30 min, and the cell aspect
637 ratio was measured at each time point. To measure the nuclear aspect ratio, embryos
638 were injected with H2B-GFP mRNA, followed by confocal live imaging at 50 hpf. Z-stack
639 images of anterior buds were acquired at 0.5 μm intervals. The nuclear aspect ratio was
640 measured using Imaris. Using the Surface tool, masks delineating the H2B-GFP signal
641 were generated at 1 μm slice intervals in the 3D images and subsequently merged to
642 reconstruct an ellipsoidal 3D nuclear structure. The lengths of the long and short axes of
643 the ellipsoid were quantified, and the nuclear aspect ratio was calculated.

644 **3) Counting cell numbers in a bud**

645 Cell counting was performed using the Mastodon plugin (https://github.com/mastodon-
646 sc/mastodon) in Fiji, which enables 3D image analysis. 3D z-stack images of the otic
647 vesicle in embryos expressing membrane-NeonGreen were acquired by confocal live
648 imaging at 0.5 or 1 μm slice intervals. Using the Big Data Viewer in the Mastodon plugin,
649 all cells in a bud were manually marked in 3D and counted. For time-lapse analysis, the
650 same buds were tracked every 30 min, and the cell number was counted at each time
651 point.

652 **4) Bud-ECM volume measurement**

653 The bud-ECM region was defined as shown in Extended Fig. 1a. 3D z-stack images of
654 the otic vesicle in embryos expressing membrane-NeonGreen were acquired by confocal
655 live imaging at 1 μm slice intervals. Bud-ECM volume was measured using Imaris

656 software. Using the Surface tool, masks delineating the bud-ECM area were generated
657 at 1 μm slice intervals in the 3D images and subsequently merged to reconstruct a 3D
658 surface filling the bud-ECM region, and the volume was quantified. For time-lapse
659 analysis, the same buds were tracked every 30 min, and the volume of bud-ECM region
660 was measured at each time point.

661 **5) Intensity analysis of multiplex in situ HCR (HCR-FISH)**

662 Measurement of the fluorescence intensity of the HCR probes was performed as
663 previously described[10]. In brief, using Fiji, maximum intensity z-projections covering the
664 entire anterior or posterior bud were created. To measure the mean intensity of HCR
665 probes, the ROI was manually drawn along the outer cells of the bud with a segmented
666 line" tool. To create a histogram plot of fluorescence intensity, regions of interest (ROIs)
667 were manually drawn using the "segmented line" tool (10 pixels wide) along the anterior
668 budding region, spanning 55-65 μm, as shown in Fig. 2. An additional 20 μm on each side
669 of the non-budding region flanking the budding cells was also included. The "plot profile"
670 tool was then used to obtain an average intensity trace along the line. Fluorescence
671 intensities were divided into 120 and 40 bins for the budding and shoulder regions,
672 respectively, expressed as normalized distances, and subsequently normalized again to
673 the overall maximum value. The Fire heatmap was used to represent the fluorescence
674 intensities of individual probes. The heatmap color scale was adjusted individually for
675 each experiment.

676 **6) Intensity analysis of the Yap1 nuclear-cytoplasm ratio**

677 For measurement of the Yap1 nuclear-to-cytoplasmic ratio in immunostained samples,
678 nuclear and cytoplasmic regions were manually segmented based on Hoechst and
679 phalloidin staining, respectively, using Fiji software, and the ratio of mean nuclear to mean
680 cytoplasmic signal intensities was calculated. For measurement using the *TgKI(Yap1-*
681 *mScarlet)* line, nuclei were manually segmented based on the H2B-GFP signal, and the
682 mean nuclear Yap1 signal intensity was quantified. The mean cytoplasmic Yap1 signal
683 intensity was obtained using the "oval" tool in Fiji by placing four circular ROIs in the

684 cytoplasm and averaging their mean intensities. The Yap1 nuclear-to-cytoplasmic ratio
685 was then calculated as described above.

686 **Statistical analysis**

687 Average values were calculated from ‘n,’ where ‘n’ represents the number of buds, bud-
688 ECM, and cells (as labeled in each figure). Plots show individual data points, mean values,
689 and error bars (standard deviation of the mean, as labeled). Before performing parametric
690 statistical tests, the Kolmogorov-Smirnov and Shapiro-Wilk tests were used to test if the
691 dataset in each experiment was from a normal distribution. To compare the difference
692 between the two groups, unpaired or paired two-tailed Student’s t-tests were performed.
693 For multiple comparisons, one-way ANOVA with Tukey’s test for normally distributed data
694 and Kruskal-Wallis test with Dunn’s test for non-normally distributed data were performed.
695 P-values less than 0.05 were considered to be significant. All statistical tests and plots
696 were made in GraphPad Prism 10.

697 **Acknowledgments**

698 We are thankful to all other members of the Principles of Tissue Morphogenesis (Munjal)
699 Lab for their feedback and support. We thank Brigid Hogan and Stefano Di Talia for their
700 critical comments on the manuscript. We thank members of the Poss and Bagnat labs for
701 valuable technical input during this project. We thank Sean Megason and Ian Swinburne
702 for their guidance and support during AM’s postdoctoral training. We thank Kazunori Ando
703 for technical support and advice to YM. We thank Toru Kawanishi and Sean Megason for
704 sharing the Yap immunostaining protocol. We thank Tony Tsai’s lab for sharing the *Yap*
705 *(4xGTIIC:EGFP)* reporter, which was not included in the final manuscript. We thank
706 Nanami Sato for illustrations. We thank the Duke Zebrafish Core Facility of the Duke
707 School of Medicine for their support. This work was funded by the National Institute of
708 Child Health and Human Development (R00HD098918 and DP2115157 to A.M.) and the
709 National Institute of Arthritis and Musculoskeletal and Skin Diseases (R01AR083346 to
710 M.B). YM is supported by JSPS Overseas Research Fellowship, Duke Regeneration

Centre Career Advancement Award, and Uehara Memorial Foundation Overseas Research Fellowship.

Author contributions

A.M. conceived and initiated the project. Y.M., with input from A.M., subsequently developed the project direction. Y.M. designed, performed, and analyzed most of the experiments with the assistance of A.M., A.B.B., and K.H. P.R. developed the theoretical model with the supervision of E.H. Y.M. generated the *Tg(hsp70l: RFP-DN-Yap1)* line, *Tg(hsp70l: DN-PKA-GFP)* line, and all constructs for the project, except those required for the *TgKI(Yap-mScarlet)* line. D.S.L. and M.B. generated the *TgKI(Yap-mScarlet)* line and the corresponding construct. J.W. analyzed the publicly available transcriptomics dataset. Y.M. and P.R. prepared figures with the input from E.H. and A.M. Y.M. and A.M. interpreted the data and wrote the original manuscript with input from P.R. and E.H. All authors reviewed and edited the manuscript. A.M. acquired funding for the project. A.M. supervised and administered the project.

Declaration of interests

The authors declare no competing interests.

References

1. Hannezo, E., and Heisenberg, C.-P. (2019). Mechanochemical Feedback Loops in Development and Disease. Cell *178*, 12–25. https://doi.org/10.1016/j.cell.2019.05.052.

2. Collinet, C., and Lecuit, T. (2021). Programmed and self-organized flow of information during morphogenesis. Nat. Rev. Mol. Cell Biol. *22*, 245–265. https://doi.org/10.1038/s41580-020-00318-6.

3. Schier, A.F. (2003). Nodal signaling in vertebrate development. Annu. Rev. Cell Dev. Biol. *19*, 589–621. https://doi.org/10.1146/annurev.cellbio.19.041603.094522.

4. Moeller, M.E., Danielsen, E.T., Herder, R., O'Connor, M.B., and Rewitz, K.F. (2013). Dynamic feedback circuits function as a switch for shaping a maturation-inducing steroid pulse in Drosophila. Development *140*, 4730–4739. https://doi.org/10.1242/dev.099739.

740 5. Vogel, V., and Sheetz, M. (2006). Integrins and Extracellular Matrix in
741 Mechanotransduction Martin Alexander Schwartz 3. Nat Rev Mol Cell Biol *7*, 265–
742 275.

743 6. Di, X., Gao, X., Peng, L., Ai, J., Jin, X., Qi, S., Li, H., Wang, K., and Luo, D. (2023).
744 Cellular mechanotransduction in health and diseases: from molecular mechanism to
745 therapeutic targets. Signal Transduct. Target. Ther. *8*, 282.
746 https://doi.org/10.1038/s41392-023-01501-9.

747 7. Dupont, S., Morsut, L., Aragona, M., Enzo, E., Giulitti, S., Cordenonsi, M., Zanconato,
748 F., Le Digabel, J., Forcato, M., Bicciato, S., et al. (2011). Role of YAP/TAZ in
749 mechanotransduction. Nature *474*, 179–183. https://doi.org/10.1038/nature10137.

750 8. Totaro, A., Panciera, T., and Piccolo, S. (2018). YAP/TAZ upstream signals and
751 downstream responses. Nat. Cell Biol. *20*, 888–899. https://doi.org/10.1038/s41556-
752 018-0142-z.

753 9. Munjal, A., Hannezo, E., Tsai, T.Y.-C., Mitchison, T.J., and Megason, S.G. (2021).
754 Extracellular hyaluronate pressure shaped by cellular tethers drives tissue
755 morphogenesis. Cell *184*, 6313-6325.e18. https://doi.org/10.1016/j.cell.2021.11.025.

756 10. Mori, Y., Smith, S., Wang, J., Eliora, N., Heikes, K.L., and Munjal, A. (2025). Versican
757 controlled by Lmx1b regulates hyaluronate density and hydration for semicircular
758 canal morphogenesis. Development *152*, dev203003.
759 https://doi.org/10.1242/dev.203003.

760 11. Whitfield, T.T. (2015). Development of the inner ear. Curr. Opin. Genet. Dev. *32*,
761 112–118. https://doi.org/10.1016/j.gde.2015.02.006.

762 12. Haddon, C.M., and Lewis, J.H. (1991). Hyaluronan as a propellant for epithelial
763 movement: the development of semicircular canals in the inner ear of Xenopus.
764 Development *112*, 541–550. https://doi.org/10.1242/dev.112.2.541.

765 13. Levic, D.S., Yamaguchi, N., Wang, S., Knaut, H., and Bagnat, M. (2021). Knock-in
766 tagging in zebrafish facilitated by insertion into non-coding regions. Development *148*.
767 https://doi.org/10.1242/dev.199994.

768 14. Geng, F.-S., Abbas, L., Baxendale, S., Holdsworth, C.J., Swanson, A.G., Slanchev,
769 K., Hammerschmidt, M., Topczewski, J., and Whitfield, T.T. (2013). Semicircular
770 canal morphogenesis in the zebrafish inner ear requires the function of gpr126
771 (lauscher), an adhesion class G protein-coupled receptor gene. Development *140*,
772 4362–4374. https://doi.org/10.1242/dev.098061.

773 15. Skouloudaki, K., Puetz, M., Simons, M., Courbard, J.-R., Boehlke, C., Hartleben, B.,
774 Engel, C., Moeller, M.J., Englert, C., Bollig, F., et al. (2009). Scribble participates in
775 Hippo signaling and is required for normal zebrafish pronephros development. Proc.
776 Natl. Acad. Sci. U. S. A. *106*, 8579–8584. https://doi.org/10.1073/pnas.0811691106.

16. Swinburne, I. (2025). A single-cell atlas of inner ear morphogenesis in zebrafish (Biorxiv 250924). (Zenodo). https://doi.org/10.5281/ZENODO.17188953 https://doi.org/10.5281/ZENODO.17188953.

17. Farrell, J.A., Wang, Y., Riesenfeld, S.J., Shekhar, K., Regev, A., and Schier, A.F. (2018). Single-cell reconstruction of developmental trajectories during zebrafish embryogenesis. Science *360*. https://doi.org/10.1126/science.aar3131.

18. Sur, A., Wang, Y., Capar, P., Margolin, G., Prochaska, M.K., and Farrell, J.A. (2023). Single-cell analysis of shared signatures and transcriptional diversity during zebrafish development. Dev. Cell *58*, 3028-3047.e12. https://doi.org/10.1016/j.devcel.2023.11.001.

19. Fernando, C.A., Conrad, P.A., Bartels, C.F., Marques, T., To, M., Balow, S.A., Nakamura, Y., and Warman, M.L. (2010). Temporal and spatial expression of CCN genes in zebrafish. Dev. Dyn. *239*, 1755–1767. https://doi.org/10.1002/dvdy.22279.

20. Yeger, H., and Perbal, B. (2016). CCN family of proteins: critical modulators of the tumor cell microenvironment. J. Cell Commun. Signal. *10*, 229–240. https://doi.org/10.1007/s12079-016-0346-6.

21. Perbal, B. (2013). CCN proteins: A centralized communication network. J. Cell Commun. Signal. *7*, 169–177. https://doi.org/10.1007/s12079-013-0193-7.

22. Zhao, B., Ye, X., Yu, J., Li, L., Li, W., Li, S., Yu, J., Lin, J.D., Wang, C.-Y., Chinnaiyan, A.M., et al. (2008). TEAD mediates YAP-dependent gene induction and growth control. Genes Dev. *22*, 1962–1971. https://doi.org/10.1101/gad.1664408.

23. Lee, S., Ahad, A., Luu, M., Moon, S., Caesar, J., Cardoso, W.V., Grant, M.B., and Chaqour, B. (2019). CCN1-Yes-Associated Protein Feedback Loop Regulates Physiological and Pathological Angiogenesis. Mol. Cell. Biol. *39*. https://doi.org/10.1128/MCB.00107-19.

24. Park, M.-H., Kim, A.K., Manandhar, S., Oh, S.-Y., Jang, G.-H., Kang, L., Lee, D.-W., Hyeon, D.Y., Lee, S.-H., Lee, H.E., et al. (2019). CCN1 interlinks integrin and hippo pathway to autoregulate tip cell activity. Elife *8*. https://doi.org/10.7554/eLife.46012.

25. Zhang, H., Pasolli, H.A., and Fuchs, E. (2011). Yes-associated protein (YAP) transcriptional coactivator functions in balancing growth and differentiation in skin. Proc. Natl. Acad. Sci. U. S. A. *108*, 2270–2275. https://doi.org/10.1073/pnas.1019603108.

26. Pocaterra, A., Romani, P., and Dupont, S. (2020). YAP/TAZ functions and their regulation at a glance. J. Cell Sci. *133*, jcs230425. https://doi.org/10.1242/jcs.230425.

27. Zanconato, F., Forcato, M., Battilana, G., Azzolin, L., Quaranta, E., Bodega, B., Rosato, A., Bicciato, S., Cordenonsi, M., and Piccolo, S. (2015). Genome-wide

813 association between YAP/TAZ/TEAD and AP-1 at enhancers drives oncogenic
814 growth. Nat. Cell Biol. *17*, 1218–1227. https://doi.org/10.1038/ncb3216.

815 28. Benhaddou, A., Keime, C., Ye, T., Morlon, A., Michel, I., Jost, B., Mengus, G., and
816 Davidson, I. (2012). Transcription factor TEAD4 regulates expression of myogenin
817 and the unfolded protein response genes during C2C12 cell differentiation. Cell
818 Death Differ. *19*, 220–231. https://doi.org/10.1038/cdd.2011.87.

819 29. Choi, H.M.T., Schwarzkopf, M., Fornace, M.E., Acharya, A., Artavanis, G., Stegmaier,
820 J., Cunha, A., and Pierce, N.A. (2018). Third-generation in situ hybridization chain
821 reaction: multiplexed, quantitative, sensitive, versatile, robust. Development *145*.
822 https://doi.org/10.1242/dev.165753.

823 30. Kurundkar, A.R., Kurundkar, D., Rangarajan, S., Locy, M.L., Zhou, Y., Liu, R.-M.,
824 Zmijewski, J., and Thannickal, V.J. (2016). The matricellular protein CCN1 enhances
825 TGF-β1/SMAD3-dependent profibrotic signaling in fibroblasts and contributes to
826 fibrogenic responses to lung injury. FASEB J. *30*, 2135–2150.
827 https://doi.org/10.1096/fj.201500173.

828 31. Nishida, T., Kawaki, H., Baxter, R.M., Deyoung, R.A., Takigawa, M., and Lyons, K.M.
829 (2007). CCN2 (Connective Tissue Growth Factor) is essential for extracellular matrix
830 production and integrin signaling in chondrocytes. J. Cell Commun. Signal. *1*, 45–58.
831 https://doi.org/10.1007/s12079-007-0005-z.

832 32. Wong, M., Kireeva, M.L., Kolesnikova, T.V., and Lau, L.F. (1997). Cyr61, product of
833 a growth factor-inducible immediate-early gene, regulates chondrogenesis in mouse
834 limb bud mesenchymal cells. Dev. Biol. *192*, 492–508.
835 https://doi.org/10.1006/dbio.1997.8766.

836 33. Mateus, R., Lourenço, R., Fang, Y., Brito, G., Farinho, A., Valério, F., and Jacinto, A.
837 (2015). Control of tissue growth by Yap relies on cell density and F-actin in zebrafish
838 fin regeneration. Development *142*, 2752–2763. https://doi.org/10.1242/dev.119701.

839 34. Jean, R.P., Gray, D.S., Spector, A.A., and Chen, C.S. (2004). Characterization of the
840 nuclear deformation caused by changes in endothelial cell shape. J. Biomech. Eng.
841 *126*, 552–558. https://doi.org/10.1115/1.1800559.

842 35. Venturini, V., Pezzano, F., Castro, F.C., Häkkinen, H.-M., Jiménez-Delgado, S.,
843 Colomer-Rosell, M., Marro, M., Tolosa-Ramon, Q., Paz-López, S., Valverde, M.A.,
844 et al. (2020). The nucleus measures shape changes for cellular proprioception to
845 control dynamic cell behavior. Science *370*, eaba2644.
846 https://doi.org/10.1126/science.aba2644.

847 36. Torregrosa-Carrión, R., Piñeiro-Sabarís, R., Siguero-Álvarez, M., Grego-Bessa, J.,
848 Luna-Zurita, L., Fernandes, V.S., MacGrogan, D., Stainier, D.Y.R., and de la Pompa,
849 J.L. (2021). Adhesion G protein-coupled receptor Gpr126/Adgrg6 is essential for
850 placental development. Sci Adv *7*, eabj5445. https://doi.org/10.1126/sciadv.abj5445.

37. Bian, F., Hansen, V., Feng, H.C., He, J., Chen, Y., Feng, K., Ebrahimi, B., Gray, R.S., Chai, Y., Wu, C.-L., et al. (2024). The G protein-coupled receptor ADGRG6 maintains mouse growth plate homeostasis through IHH signaling. J. Bone Miner. Res. *39*, 1644–1658. https://doi.org/10.1093/jbmr/zjae144.

38. Pogoda, H.-M., Sternheim, N., Lyons, D.A., Diamond, B., Hawkins, T.A., Woods, I.G., Bhatt, D.H., Franzini-Armstrong, C., Dominguez, C., Arana, N., et al. (2006). A genetic screen identifies genes essential for development of myelinated axons in zebrafish. Dev. Biol. *298*, 118–131. https://doi.org/10.1016/j.ydbio.2006.06.021.

39. Mogha, A., Benesh, A.E., Patra, C., Engel, F.B., Schöneberg, T., Liebscher, I., and Monk, K.R. (2013). Gpr126 functions in Schwann cells to control differentiation and myelination via G-protein activation. J. Neurosci. *33*, 17976–17985. https://doi.org/10.1523/JNEUROSCI.1809-13.2013.

40. Petersen, S.C., Luo, R., Liebscher, I., Giera, S., Jeong, S.-J., Mogha, A., Ghidinelli, M., Feltri, M.L., Schöneberg, T., Piao, X., et al. (2015). The adhesion GPCR GPR126 has distinct, domain-dependent functions in Schwann cell development mediated by interaction with laminin-211. Neuron *85*, 755–769. https://doi.org/10.1016/j.neuron.2014.12.057.

41. Seamon, K., and Daly, J.W. (1981). Activation of adenylate cyclase by the diterpene forskolin does not require the guanine nucleotide regulatory protein. J. Biol. Chem. *256*, 9799–9801. https://doi.org/10.1016/s0021-9258(19)68694-1.

42. Gonzalez, G.A., and Montminy, M.R. (1989). Cyclic AMP stimulates somatostatin gene transcription by phosphorylation of CREB at serine 133. Cell *59*, 675–680. https://doi.org/10.1016/0092-8674(89)90013-5.

43. Dobroff, A.S., Wang, H., Melnikova, V.O., Villares, G.J., Zigler, M., Huang, L., and Bar-Eli, M. (2009). Silencing cAMP-response element-binding protein (CREB) identifies CYR61 as a tumor suppressor gene in melanoma. J. Biol. Chem. *284*, 26194–26206. https://doi.org/10.1074/jbc.M109.019836.

44. Yu, Z., Kong, Q., and Kone, B.C. (2010). CREB trans-activation of disruptor of telomeric silencing-1 mediates forskolin inhibition of CTGF transcription in mesangial cells. Am. J. Physiol. Renal Physiol. *298*, F617-24. https://doi.org/10.1152/ajprenal.00636.2009.

45. Inhibition Protein Kinase Phenocopies Ectopic Expression ofhedgehogin CNS Wild-Type andcyclopsMutant Embryos.

46. Aragona, M., Panciera, T., Manfrin, A., Giulitti, S., Michielin, F., Elvassore, N., Dupont, S., and Piccolo, S. (2013). A mechanical checkpoint controls multicellular growth through YAP/TAZ regulation by actin-processing factors. Cell *154*, 1047–1059. https://doi.org/10.1016/j.cell.2013.07.042.

47. Mason, D.E., Collins, J.M., Dawahare, J.H., Nguyen, T.D., Lin, Y., Voytik-Harbin, S.L., Zorlutuna, P., Yoder, M.C., and Boerckel, J.D. (2019). YAP and TAZ limit cytoskeletal and focal adhesion maturation to enable persistent cell motility. J. Cell Biol. *218*, 1369–1389. https://doi.org/10.1083/jcb.201806065.

48. Mason, D.E., Goeckel, M., Vega, S.L., Wu, P.-H., Johnson, D., Heo, S.-J., Wirtz, D., Burdick, J.A., Wood, L., Chow, B., et al. (2023). Mechanotransductive feedback control of endothelial cell motility and vascular morphogenesis. https://doi.org/10.7554/elife.86668.1.

49. Panciera, T., Azzolin, L., Cordenonsi, M., and Piccolo, S. (2017). Mechanobiology of YAP and TAZ in physiology and disease. Nat. Rev. Mol. Cell Biol. *18*, 758–770. https://doi.org/10.1038/nrm.2017.87.

50. Lau, L.F. (2016). Cell surface receptors for CCN proteins. J. Cell Commun. Signal. *10*, 121–127. https://doi.org/10.1007/s12079-016-0324-z.

51. Wang, X., Li, L., and Liu, D. (2014). Expression analysis of integrin β1 isoforms during zebrafish embryonic development. Gene Expr. Patterns *16*, 86–92. https://doi.org/10.1016/j.gep.2014.10.001.

52. Littlewood Evans, A., and Müller, U. (2000). Stereocilia defects in the sensory hair cells of the inner ear in mice deficient in integrin alpha8beta1. Nat. Genet. *24*, 424–428. https://doi.org/10.1038/74286.

53. Kechagia, J.Z., Ivaska, J., and Roca-Cusachs, P. (2019). Integrins as biomechanical sensors of the microenvironment. Nat. Rev. Mol. Cell Biol. *20*, 457–473. https://doi.org/10.1038/s41580-019-0134-2.

54. Monk, K.R., Oshima, K., Jörs, S., Heller, S., and Talbot, W.S. (2011). Gpr126 is essential for peripheral nerve development and myelination in mammals. Development *138*, 2673–2680. https://doi.org/10.1242/dev.062224.

55. Patra, C., van Amerongen, M.J., Ghosh, S., Ricciardi, F., Sajjad, A., Novoyatleva, T., Mogha, A., Monk, K.R., Mühlfeld, C., and Engel, F.B. (2013). Organ-specific function of adhesion G protein-coupled receptor GPR126 is domain-dependent. Proc. Natl. Acad. Sci. U. S. A. *110*, 16898–16903. https://doi.org/10.1073/pnas.1304837110.

56. Lu, S., Liu, S., Wietelmann, A., Kojonazarov, B., Atzberger, A., Tang, C., Schermuly, R.T., Gröne, H.-J., and Offermanns, S. (2017). Developmental vascular remodeling defects and postnatal kidney failure in mice lacking Gpr116 (Adgrf5) and Eltd1 (Adgrl4). PLoS One *12*, e0183166. https://doi.org/10.1371/journal.pone.0183166.

57. Lala, T., and Hall, R.A. (2022). Adhesion G protein-coupled receptors: structure, signaling, physiology, and pathophysiology. Physiol. Rev. *102*, 1587–1624. https://doi.org/10.1152/physrev.00027.2021.

58. Paavola, K.J., Sidik, H., Zuchero, J.B., Eckart, M., and Talbot, W.S. (2014). Type IV collagen is an activating ligand for the adhesion G protein-coupled receptor GPR126. Sci. Signal. *7*, ra76. https://doi.org/10.1126/scisignal.2005347.

59. Mitgau, J., Franke, J., Schinner, C., Stephan, G., Berndt, S., Placantonakis, D.G., Kalwa, H., Spindler, V., Wilde, C., and Liebscher, I. (2022). The N Terminus of Adhesion G Protein-Coupled Receptor GPR126/ADGRG6 as Allosteric Force Integrator. Front Cell Dev Biol *10*, 873278. https://doi.org/10.3389/fcell.2022.873278.

60. Li, Q., Huo, A., Li, M., Wang, J., Yin, Q., Chen, L., Chu, X., Qin, Y., Qi, Y., Li, Y., et al. (2024). Structure, ligands, and roles of GPR126/ADGRG6 in the development and diseases. Genes Dis *11*, 294–305. https://doi.org/10.1016/j.gendis.2023.02.016.

61. Wilde, C., Mitgau, J., Suchý, T., Schöneberg, T., and Liebscher, I. (2022). Translating the force-mechano-sensing GPCRs. Am. J. Physiol. Cell Physiol. *322*, C1047–C1060. https://doi.org/10.1152/ajpcell.00465.2021.

62. Behrndt, M., Salbreux, G., Campinho, P., Hauschild, R., Oswald, F., Roensch, J., Grill, S.W., and Heisenberg, C.-P. (2012). Forces driving epithelial spreading in zebrafish gastrulation. Science *338*, 257–260. https://doi.org/10.1126/science.1224143.

63. Gerety, S.S., and Wilkinson, D.G. (2011). Morpholino artifacts provide pitfalls and reveal a novel role for pro-apoptotic genes in hindbrain boundary development. Dev. Biol. *350*, 279–289. https://doi.org/10.1016/j.ydbio.2010.11.030.

64. Sorlien, E.L., Witucki, M.A., and Ogas, J. (2018). Efficient Production and Identification of CRISPR/Cas9-generated Gene Knockouts in the Model System Danio rerio. J. Vis. Exp. https://doi.org/10.3791/56969.

65. Stuart, T., Butler, A., Hoffman, P., Hafemeister, C., Papalexi, E., Mauck, W.M., III, Hao, Y., Stoeckius, M., Smibert, P., and Satija, R. (2019). Comprehensive integration of single-cell data. Cell *177*, 1888-1902.e21. https://doi.org/10.1016/j.cell.2019.05.031.

66. Blondel, V.D., Guillaume, J.-L., Lambiotte, R., and Lefebvre, E. (2008). Fast unfolding of communities in large networks. J. Stat. Mech. *2008*, P10008. https://doi.org/10.1088/1742-5468/2008/10/p10008.

67. Schultz, J., Milpetz, F., Bork, P., and Ponting, C.P. (1998). SMART, a simple modular architecture research tool: identification of signaling domains. Proc. Natl. Acad. Sci. U. S. A. *95*, 5857–5864. https://doi.org/10.1073/pnas.95.11.5857.

68. Letunic, I., Khedkar, S., and Bork, P. (2021). SMART: recent updates, new developments and status in 2020. Nucleic Acids Res. *49*, D458–D460. https://doi.org/10.1093/nar/gkaa937.

960 69. Sievers, F., and Higgins, D.G. (2014). Clustal Omega, accurate alignment of very
961 large numbers of sequences. Methods Mol. Biol. *1079*, 105–116.
962 https://doi.org/10.1007/978-1-62703-646-7_6.

Figure Legends

Figure 1: ECM swelling-mediated Yap activation is required for bud extension

(a) Three-dimensional (3D) rendered OVs imaged at selected time points using *Tg(actb2:membrane-neongreen-neongreen)* embryos. A, anterior bud; AL, anterior-lateral bud; P, posterior bud; PL, posterior-lateral bud; V, ventral bud. Developmental stages shown in hours post fertilization (hpf). Scale bar: 50 μm.

(b-b') 2D sections of OVs imaged at selected time points using H2B-GFP mRNA injected *TgKI(Yap1-mScarlet)* embryos. Insets (b') show enlarged images of the anterior pre-budding or budding region corresponding to the white boxes in (b). Dorsal epithelial cells showing nuclear-Yap localization are indicated by asterisks. Scale bar: 10 or 50 μm. Representative images from three independent experiments are shown.

(c) Quantification of the Yap nuclear to cytoplasmic ratio in the cells at the anterior pre-budding or budding region at selected time points. Data are mean ± SD. *n* denotes the number of cells measured per condition from seven individual embryos from three independent experiments. *P*-value as labeled (Mann-Whitney test).

(d-e) Effect of hyaluronidase injection on Yap nuclear translocation. (d) 2D sections of the anterior bud in *TgKI(Yap1-mScarlet)*, injected with H2B-GFP mRNA, imaged before and at 1.5 h post-injection (hpi) of PBS or HAase. Pre-injection and post-injection images were acquired from the same individual embryos. Arrows indicate Yap1 translocated to the nucleus. Scale bar: 10 μm. Representative images from two independent experiments are shown. (d) Quantification of the Yap nuclear to cytoplasmic ratio in the anterior bud before and at 1.5 hpi of PBS or HAase. Data are mean ± SD. *n* denotes the number of cells measured per condition from ten individual embryos from two independent experiments. *P*-values as labeled (Kruskal–Wallis test with Dunn's test).

(f-g) Effect of *yap1* knockdown on bud growth. (f) 3D-rendered OVs from from *Tg(actb2:membrane-neongreen-neongreen)* embryos, injected with control or *yap1* MO, imaged at 50 hpf. Scale bar: 50 μm. Representative images from two independent experiments are shown. (g) Quantification of bud length in embryos injected with control or *yap1* MO at 50 hpf. Data are mean ± SD. *n* denotes the number of buds from individual embryos measured per condition from two independent experiments. *P*-values as labeled (unpaired two-tailed Student's t-test)

Figure 2: *ccn1l1*, a Yap target gene, is enriched in the canal genesis zone during SCC formation

(a) UMAP of single-cell RNA of the inner ear cell clusters from the DanioCell dataset. Single cells in the canal-forming cell cluster are colored blue.

(b) Dot plot showing the expression levels of the top 10 DEGs in the canal-forming cell cluster during SCC formation: pre-budding (36-40 hpf), bud extension (45-50 hpf), and bud fusion (60-72 hpf) stages. Color encodes the normalized gene expression level, and the dot size encodes the percentage of positive cells within a cluster.

(c) 3D-rendered OVs at select time points stained with multiplex *in situ* probes against *ccn1l1* (green) and *col2a1a* (white). Scale bar: 50 µm. Representative images from three independent experiments are shown.

(d) Normalized fluorescence probe intensities of *ccn1l1* or *col2a1a* genes across the illustrated region of interest (ROI) at 50 hpf indicated by the red dashed line along the anterior bud. Data are mean ± SEM. *n* denotes the number of buds from individual embryos measured per condition from three independent experiments.

(e) Comparison of normalized fluorescence probe intensity of *ccn1l1* in the anterior pre-budding, budding, or pillar region at each stage. Data are mean ± SD. *n* denotes the number of buds or pillars from individual embryos measured from two independent experiments. *P*-values as labeled (one-way ANOVA with Tukey's test).

(f-g) Effect of *yap1* knockdown on *ccn1l1* expression. (f) 3D-rendered OVs from *Tg(actb2:membrane-neongreen-neongreen)* embryos at 50 hpf stained with multiplex *in situ* probes against *ccn1l1* (green). Heatmap represents fluorescence intensity with the same contrast for the *ccn1l1* probe of embryos injected with control and *yap1* MO. Scale bar: 50 µm. Representative images from two independent experiments are shown. (g) Quantification of probe fluorescence intensity of *ccn1l1* probe in anterior buds. Data are mean ± SD. *n* denotes the number of buds from individual embryos measured from two independent experiments. *P*-value as labeled (unpaired two-tailed Student's t-test).

Figure 3: Ccn1l1 induces ECM production and drives positive feedback loop via Yap mechanotransduction

(a-b) Effect of *ccn1l1* knockdown on bud growth. (a) 3D-rendered OVs from *Tg(actb2:membrane-neongreen-neongreen)* embryos, injected with *tyrosinase* gRNA, *ccn1l1* gRNA, control MO or *ccn1l1* MO, imaged at 50 hpf. Scale bar: 50 µm. Representative images from three independent experiments are shown. *tyrosinase* gRNA is used as a gRNA injection control because it causes loss of pigmentation but does not affect SCC formation. (b) Quantification of bud length in control or *ccn1l1* knockdown embryos at 50 hpf. Data are mean ± SD. In the absence of buds, bud

lengths correspond to cell height. *n* denotes the number of buds from individual embryos measured per condition from three independent experiments. *P*-values as labeled (unpaired two-tailed Student's t-test).

(c-d) Effect of *ccn1l1* knockdown on *has3* and *vcanb* expression levels in buds. (c) 3D-rendered OVs at 50 hpf stained with multiplex *in situ* probes against *has3* (green), *vcanb* (magenta), and *col2a1a* (white). Heatmaps represent fluorescence intensity with the same contrast for each probe of embryos injected with control or *ccn1l1* MO. Scale bar: 50 µm. Representative images from two independent experiments are shown. (d) Quantification of probe fluorescence intensity of *has3* or *vcanb* probe in anterior buds. Data are mean ± SD. *n* denotes the number of buds from individual embryos measured per condition from two independent experiments. *P*-values as labeled (unpaired two-tailed Student's t-test).

(e-h) Effect of hyaluronidase injection on *ccn1l1* and *has3* expression levels in buds. 3D-rendered OVs and quantification of probe fluorescence intensity of *ccn1l1* (e-f) or *has3* (g-h) at 0 or 6 hpi of PBS or HAase. Heatmaps represent fluorescence intensity with the same contrast for each probe of embryos injected with PBS or HAase. Scale bar: 50 µm. Representative images from two independent experiments are shown. Data are mean ± SD. *n* denotes the number of buds from individual embryos measured per condition from two independent experiments. *P*-values as labeled (one-way ANOVA with Tukey's test).

(i-k) Effect of DN Yap1 expression on bud extension and bud-ECM volume. (i) 2D sections of anterior buds from *Tg(hsp: RFP-DN Yap1)* and sibling control embryos, both *Tg(actb2:membrane-neongreen-neongreen)*, imaged at 50 hpf following heat-shock induction. Regions marked in light blue indicate the bud-ECM region measured in quantifications. Scale bar: 20 µm. Representative images from two independent experiments are shown. Quantification of bud length (j) and bud-ECM volume (k) in sibling control or DN Yap1-expressing embryos at 50 hpf. Data are mean ± SD. *n* denotes the number of buds from individual embryos measured per condition from two independent experiments. *P*-values as labeled (unpaired two-tailed Student's t-test).

(l) A schematic model of the positive mechanotransduction feedback loop during bud growth.

Figure 4: Mechanical patterning by the positive feedback loop recruits adjacent cells to sustain bud extension and ensure timely

(a) Quantification of cell number in the anterior bud across individual time points obtained from time-lapse imaging of *Tg(actb2:membrane-neongreen-neongreen)* embryos. Data are mean ± SD. Dashed lines indicate the range of SD at each time

point. *n* denotes the number of buds from individual embryos measured from three independent experiments.

(b) 3D-rendered images of an anterior bud of the *Tg(actb2:membrane-neongreen-neongreen)* embryo at selected time points with individual cells tracked. Scale bar: 50 μm. Representative images from two independent experiments are shown.

(c) Quantification of cell number in anterior buds of embryos injected with PBS or HAase at 0 or 6 hpi. Data are mean ± SD. *n* denotes the number of buds from individual embryos measured per condition from two independent experiments. *P*-values as labeled (one-way ANOVA with Tukey's test).

(d) Quantification of cell number in anterior buds of embryos injected with control or *yap1* MO at 50 hpf. Data are mean ± SD. *n* denotes the number of buds from individual embryos measured per condition from two independent experiments. *P*-value as labeled (unpaired two-tailed Student's t-test).

(e) Schematics of the 2D vertex model simulations, showing tip, budding and border cells, as well as the relevant physical parameters. All values of physical parameters are given in the supplementary information.

(f) Trajectories of the aspect ratio of a tip cell and a recruited cell obtained with 2D vertex model simulations, exhibiting a sharp increase in aspect ratio as cell position shifts from the bud border to the budding region. Illustrations show trajectories of two individual cells from bud initiation to the end of bud extension (defined by the moment where the bud height reaches 30 μm).

(g) Quantification of 3D nuclear aspect ratio. The nuclear aspect ratio was calculated as the ratio of the long to short axes (long/short) of the ellipsoidal nucleus. Data are mean ± SD. *n* denotes the number of nuclei from individual cells measured per condition from one experiment. *P*-value as labeled (unpaired two-tailed Student's t-test).

(h) Spatial difference of Yap nuclear translocation within the anterior bud at 50 hpf. Data are mean ± SD. coefficient of variation (CV) of each condition is shown. *n* denotes the number of cells per condition from two independent experiments. *P*-values as labeled (one-way ANOVA with Tukey's test).

(i) Simulation of bud-ECM area over time, with and without mechanotransduction-driven ECM production. Tip cells are set to 100% ECM production rate.

(j) Quantification of bud-ECM volume of anterior buds in embryos injected with control or *yap1* MO at selected time points. Data are mean ± SD. *n* denotes the number of cells per condition from two independent experiments. *P*-values at selected time pointes as labeled (unpaired two-tailed Student's t-test).

(k) Simulation of bud length over time, with and without mechanotransduction-driven ECM production. Tip cells are set to 100% ECM production rate.

(l) Quantification of bud length of the anterior buds in embryos injected with control or *yap1* MO at selected time points. Data are mean ± SD. *n* denotes the number of cells per condition from two independent experiments. *P*-values at selected time points as labeled (unpaired two-tailed Student's t-test).

(m) Phase diagram showing the time needed for the bud to reach 30 μm and fuse, as a function of bud ECM production by budding cells (x axis) and tip cells (y axis). The dotted level line indicates the region where fusion happens in less than 15 hours after budding. Grey areas indicate regions where the bud failed to fuse (did not reach 30 μm within 22 hours after budding).

(n) Quantification of bud growth rate (μm/hour) of the anterior bud in wild-type embryos or embryos injected with *ccn1l1* MO. Data are mean ± SD. *n* denotes the number of cells per condition from one experiment. *P*-values as labeled (one-way ANOVA with Tukey's test). Growth rates for each bud were calculated over the following time ranges during bud extension stage: control (48-50 hpf); *ccn1l1* MO 0.5, 1, and 2 ng (50-56 hpf).

(o) 3D-rendered OVs from *Tg(actb2:membrane-neongreen-neongreen)* embryos, injected with control or *ccn1l1* MO, imaged at selected time points. Scale bar: 50 μm. Representative images from one experiment per condition are shown.

Figure 5: Gpr126-cAMP-PKA-CREB signaling during bud fusion suppresses *ccn1l1* expression to terminate bud extension

(a) 3D-rendered OVs from wild-type or *gpr126* $^{st49/st49}$ mutant embryos, both *Tg(actb2:membrane-neongreen-neongreen),* imaged at selected time points. Blue and yellow dashed lines indicate the anterior bud/pillar or the anterior-lateral portion of the pillar, respectively. Scale bar: 50 μm. Representative images from two independent experiments are shown.

(b-c) *ccn1l1* and *has3* expression levels in *gpr126* $^{st49/st49}$ mutant embryos. (b) 3D-rendered OVs of wild-type or *gpr126* $^{st49/st49}$ mutant embryos at 60 hpf stained with multiplex *in situ* probes against *ccn1l1* (green), *has3* (magenta), and *col2a1a* (white). Heatmaps represent fluorescence intensity with the same contrast for each probe of embryos. Scale bar: 50 μm. Representative images from three independent experiments are shown. (c) Quantification of probe fluorescence intensities of *ccn1l1* or *has3* probes in anterior buds or pillars at 50 hpf or 60 hpf. Data are mean ± SD. *n* denotes the number of buds or pillars from individual embryos measured from three independent experiments. *P*-values as labeled (Kruskal-Wallis test with Dunn's test).

(d-f) Effect of *gpr126* $^{st49/st49}$ mutation on bud growth. Quantification of bud length (d), cell number in the anterior bud or pillar (e), and bud-ECM volume (f) at selected time points. Data are mean ± SD. *n* denotes the number of buds or pillars from individual embryos measured from two independent experiments. *P*-values as labeled (unpaired two-tailed Student's t-test).

(g) 2D sections of OVs showing phospho-CREB and F-actin, stained using anti-phospho-CREB^{ser133} antibody and phalloidin, respectively, at selected time points. Insets show enlarged images of the anterior buds corresponding to the dashed white boxes. Scale bar: 50 μm. Representative images from three independent experiments are shown.

(h) 2D sections OVs showing phospho-CREB and F-actin, stained using anti-phospho-CREB^{ser133} antibody and phalloidin, respectively, at 60 hpf in sibling control or *gpr126* $^{st49/st49}$ mutant embryos. Scale bar: 50 μm. Representative images from two independent experiments are shown.

(i-j) Effect of DN PKA on *ccn1l1* expression in buds. (i) 3D-rendered OVs from *Tg(hsp:DN PKA-GFP)* embryos and sibling controls after heat-shock induction, stained with multiplex *in situ* probes against *ccn1l1* (magenta) and *col2a1a* (white). Heatmaps represent fluorescence intensity with the same contrast for the *ccn1l1* probe of each. Scale bar: 50 μm. Representative images from three independent experiments are shown. (j) Quantification of probe fluorescence intensity of *ccn1l1* in anterior buds or pillars at 56 hpf. Data are mean ± SD. *n* denotes the number of buds or pillars from individual embryos measured from three independent experiments. *P*-value as labeled (unpaired two-tailed Student's t-test).

Extended Figure Legends

Extended Figure 1: ECM swelling-mediated Yap activation in budding cells, related to Figure 1

(a) Illustration of budding epithelium and bud-ECM region filled with hyaluronan.

(b) 3D-rendered and 2D section of the anterior bud imaged at budding (45 hpf) and bud extension (50 hpf) stages using *Tg(actb2:membrane-neongreen-neongreen)* embryos. Yellow asterisk indicates the opposing anterior-lateral bud. Regions marked in light blue indicate the bud-ECM region. Scale bar: 20 μm. Representative images from two independent experiments are shown.

(c) Quantification of cell aspect ratio in budding cells in the anterior bud at budding (45 hpf) and bud extension (50 hpf) stages. Cell height and width in a budding cell are defined as described in Extended Fig. 1a. Data are mean ± SD. *n* denotes the number of buds from individual embryos measured per condition from two independent experiments. *P*-value as labeled (unpaired two-tailed Student's t-test).

(d) Quantification of the Yap nuclear to cytoplasmic ratio in the dorsal epithelial cells at pre-budding (40 hpf) or bud extension (50 hpf) stages. Data are mean ± SD. *n* denotes the number of cells measured per condition from nine individual embryos of two independent experiments. *P*-value as labeled (unpaired two-tailed Student's t-test).

(e) 2D sections of the anterior bud in *Tg(actb2:membrane-neongreen-neongreen)* embryos imaged at 0 and 6 hpi of PBS and HAase. 0 hpi and 6 hpi images were acquired from the same embryo. Scale bar: 20 μm. Representative images from two independent experiments are shown.

(f) Quantification of bud-ECM volume of PBS or HAase-treated anterior buds at 6 hpi (52 hpf). Data are mean ± SD. *n* denotes the number of buds measured per condition from two independent experiments. *P*-value as labeled (unpaired two-tailed Student's t-test).

(g) Quantification of cell aspect ratio of budding cells in anterior buds before (46 hpf) and at 6 hpi (52 hpf) of PBS and HAase. Data are mean ± SD. *n* denotes the number of buds from individual embryos measured per condition from two independent experiments. *P*-values as labeled (Kruskal-Wallis test with Dunn's test).

(h) Quantification of bud length of anterior buds before (46 hpf) and at 6 hpi (52 hpf) of PBS and HAase. Data are mean ± SD. *n* denotes the number of buds from individual embryos measured per condition from two independent experiments. *P*-values as labeled (one-way ANOVA with Tukey's test).

(i) Quantification of the Yap nuclear-cytoplasmic ratio in the dorsal epithelial cells before (50 hpf) and after (51.5 hpf) injection of HAase. Data are mean ± SD. *n* denotes the number of cells measured per condition from nine individual embryos of two independent experiments. *P*-value as labeled (Mann-Whitney test).

(j-k) Immunostaining of Yap1 in budding cells. (j) 2D sections of anterior buds showing Yap1 and nuclear staining using anti-Yap1 antibody and Hoechst stain respectively, at selected time points. Scale bar: 10 μm. Arrows indicate Yap1 translocated to the nucleus. Representative images from two independent experiments are shown. (k) Quantification of the Yap nuclear-cytoplasmic ratio in the epithelial cells at the canal genesis zone at selected time points. Data are mean ± SD. *n* denotes the number of cells measured per condition from two independent experiments. *P*-values as labeled (Kruskal-Wallis test with Dunn's test).

(l-m) Effect of HAase on nuclear Yap translocation. (l) 2D sections of anterior buds showing Yap1 and nuclear staining using anti-Yap1 antibody, and Hoechst stain, respectively, at 3 hpi of PBS or HAase. Scale bar: 10 μm. Arrows indicate Yap1 translocated to the nucleus. Representative images from two independent experiments are shown. (m) Quantification of the Yap nuclear to cytoplasmic ratio in the budding cells in the anterior buds at 3 hpi of PBS or HAase. Data are mean ± SD. *n* denotes the number of cells measured per condition from two independent experiments. *P*-value as labeled (Mann-Whitney test).

(n) 3D-rendered OVs from *Tg(actb2:membrane-neongreen-neongreen)* embryos, injected with control or *yap1* MO, imaged at 72 hpf. Yellow arrows indicate unfused posterior and ventral buds. Scale bar: 50 μm. Representative images from three independent experiments are shown.

Extended Figure 2: Lmx1bb regulates *ccn1l1* expression at the canal genesis zone, related to Figure 2

(a) UMAP of single-cell RNA of *vcanb*-expressing cell cluster from the DanioCell dataset. Heatmap color of each dot represents *vcanb* expression levels.

(b) Schematic image and sequence of the TEAD binding motifs in the genomic sequence upstream of the *ccn1l1* locus.

(c-d) Effect of *yap1* knockdown on the onset of *ccn1l1* expression at the pre-budding stage. (c) 3D-rendered OVs, injected with control or *yap1* MO, imaged at 40 hpf stained with multiplex *in situ* probes against *ccn1l1* (green) and *col2a1a* (white). Scale bar: 50 μm. Representative images from two independent experiments are shown. (d) Quantification of probe fluorescence intensity of *ccn1l1* probe in the anterior budding region at the pre-budding stage (40 hpf). Data are mean ± SD. *n* denotes the number of budding regions from individual embryos measured from two independent experiments. *P*-value as labeled (unpaired two-tailed Student's t-test).

(e-f) Effect of *lmx1bb* mutation on *ccn1l1* expression level. (e) 3D-rendered OVs of *lmx1bb* $^{jj410/jj410}$ or sibling control embryos at 50 hpf stained with multiplex *in situ* probes against *ccn1l1* (green) and *col2a1a* (white). Heatmap represents fluorescence intensity with the same contrast for the *ccn1l1* probe of each. Scale bar: 50 μm. Representative images from three independent experiments are shown. (f) Quantification of probe fluorescence intensity of *ccn1l1* probe in the posterior pre-budding region. Data are mean ± SD. *n* denotes the number of budding regions from individual embryos measured from two independent experiments. *P*-value as labeled (unpaired two-tailed Student's t-test).

(g) Maximum intensity projections of OVs treated with Notch receptor inhibitor RO4929097 at 50 hpf stained with multiplex *in situ* probes against *lmx1bb* (magenta), *ccn1l1* (green), and *col2a1a* (white). Scale bar: 50 µm. Representative images from three independent experiments are shown.

Extended Figure 3: Ccn1l1 induces *has3* and *vcanb* expression in budding cells, related to Figure 3

(a) E-values of predicted functional domains of zebrafish Ccn1l1 obtained with SMART.

(b) Multiple sequence alignment of amino acids of each functional domain from zebrafish (*Danio rerio*) Ccn1l1 (Dr_Ccn1l1), zebrafish Ccn1 (Dr_Ccn1), and human (*Homo sapiens*) CCN1 (Hs_CCN1) performed with Clustal Omega. Black (*), dark grey (:), and grey (.) indicate fully conserved residues, strong similarity of residues, and weak similarity of residues, respectively, across species. The percentage sequence identity of Dr_Ccn1 and Dr_Ccn1l1 relative to Hs_CCN1 is shown.

(c) 3D-rendered OVs at pre-budding (40 hpf) or bud extension (50 hpf) stages stained with multiplex *in situ* probes against *ccn1l1* (cyan), *has3* (green), and *vcanb* (green). A, anterior bud; AL, anterior-lateral bud; P, posterior bud; PL, posterior-lateral bud; V, ventral bud. Scale bar: 50 µm. Representative images from three independent experiments are shown.

(d) Quantification of probe fluorescence intensities of *has3 and vcanb* probe measured at the pre-budding stage (anterior budding region), extension stage (anterior bud region), or fusion stage (anterior pillar region). Data are mean ± SD. *n* denotes the number of buds from individual embryos measured from two independent experiments.

(e-f) Effect of *ccn1l1* knockdown on *has3* and *vcanb* expression at the pre-budding stage. (e) 3D-rendered OVs injected with control or *ccn1l1* MO at 40 hpf stained with multiplex *in situ* probes against *has3* (green), *vcanb* (magenta), and *col2a1a* (white). Heatmaps represent fluorescence intensity with the same contrast for each probe of embryos. Scale bar: 50 µm. Representative images from two independent experiments are shown. (f) Quantification of probe fluorescence intensites of *has3* and *vcanb* probes in the anterior pre-budding region. Data are mean ± SD. *n* denotes the number of buds from individual embryos measured from two independent experiments. *P*-values as labeled (unpaired two-tailed Student's t-test).

Extended Figure 4: Mechanical patterning of budding cells, related to Figure 4

(a) Simulation snapshot of a bud with low adhesion to the basement membrane obtained with the 2D vertex model, showing the trajectory of two cells during bud extension. Upper and lower panels show the bud shape after and before budding, respectively.

(b) Simulated aspect ratio of a tip cell and a recruited cell during bud extension, in the case of low adhesion to the basement membrane. The dashed black line indicates the trajectory of the aspect ratio of a recruited cell in the control case.

(c) Simulation snapshot of a bud in the absence of cytocinches obtained with the 2D vertex model, showing the trajectory of two cells during bud extension. Cells appear to be pushed away from the bud center, rather than flowing towards it. Upper and lower panels show the bud shape after and before budding, respectively.

(d) Simulated Aspect ratio of a tip cell and a recruited cell during bud extension obtained with the 2D vertex model, in the absence of cytocinches. The dashed black line indicates the evolution of the aspect ratio of a recruited cell in the control case.

(e) Simulation snapshots of bud morphology at 5 hours post-budding for different ECM production rate parameter values. The red heat map shows the ECM production rate in tip cells. Mech. t. indicates the percent of ECM production driven by mechanotransduction contribution from recruited cells.

(f) 2D sections of anterior buds from *Tg(actb2:membrane-neongreen-neongreen)* embryos injected with control or *ccn1l1* MO at the indicated concentrations, imaged at 50 hpf. Scale bar: 20 μm. Representative images from two independent experiments are shown.

Extended Figure 5: Gpr126-cAMP-PKA-CREB signaling terminates bud extension, related to Figure 5

(a) Quantification of anterior bud length across individual time points obtained from time-lapse imaging of *Tg(actb2:membrane-neongreen-neongreen)* embryos. Data are mean ± SD. Dashed lines indicate the range of SD at each time point. *n* denotes the number of buds from individual embryos measured from three independent experiments.

(b) 3D-rendered OVs at selected time points stained with multiplex *in situ* probes against *gpr126* (green) and *col2a1a* (white). Heatmap represents fluorescence intensity with the same contrast for the *gpr126* probe of each embryo. Scale bar: 50 μm. Representative images from two independent experiments are shown.

(c) 3D-rendered OVs of wild-type and *gpr126* $^{st49/st49}$ mutant embryos at 72 hpf stained with multiplex *in situ* probes against *ccn1l1* (green), *has3* (magenta), and *col2a1a* (white). Heatmaps represent fluorescence intensity with the same contrast for each

probe of wild-type or *gpr126* $^{st49/st49}$ mutant embryos. Scale bar: 50 µm. Representative images from three independent experiments are shown.

(d) Quantification of bud-ECM volume in anterior buds across individual time points obtained from time-lapse imaging of wild-type or *gpr126* $^{st49/st49}$ embryos expressing membrane-NeonGreen. Data are mean ± SD. *n* denotes the number of buds from individual embryos measured from three independent experiments. *P*-values as labeled (unpaired two-tailed Student's t-test)

(e) Simulated bud ECM area (equivalent of bud ECM volume in our 2D simulation) as function of time, with (fusion: blue line) or in the absence (no fusion: red line) of the terminating event of bud fusion. Tip and budding cell productions are set to 100%.

(f-g) Effect of forskolin treatment on *ccn1l1* and *has3* expression. (f) 3D-rendered OVs of embryos treated with forskolin at 52 hpf stained with multiplex *in situ* probes against the combination of *ccn1l1* (green) and *col2a1a* (white) or *has3* (magenta) and *col2a1a* (white). Scale bar: 50 µm. Representative images from two independent experiments are shown. (g) Quantification of probe fluorescence intensities of the *ccn1l1* and *has3* probes in the anterior bud. Data are mean ± SD. *n* denotes the number of buds from individual embryos measured from two independent experiments. *P*-values as labeled (unpaired two-tailed Student's t-test).

(h-i) Effect of forskolin treatment on bud growth. (h) 3D-rendered OVs of *Tg(actb2:membrane-neongreen-neongreen)* embryos, treated with forskolin, imaged at 52 hpf. Scale bar: 50 µm. Representative images from two independent experiments are shown. (i) Quantification of bud length in embryos treated with forskolin at 52 hpf. Data are mean ± SD. *n* denotes the number of buds from individual embryos measured per condition from two independent experiments. *P*-value as labeled (unpaired two-tailed Student's t-test).

(j) 2D sections of OVs showing phospho-CREB, DN PKA-GFP and F-actin staining using anti-phospho-CREB^{ser133} antibody, anti-GFP antibody, and phalloidin, respectively, at 56 hpf in sibling control or in DN PKA-GFP-expressing embryos following heat-shock induction. Scale bar: 50 µm. Representative images from two independent experiments are shown.

(k) 3D-rendered OVs from *Tg(hsp: DN PKA-GFP)* and sibling control embryos, both *Tg(βActin: utrophin-mCherry*, imaged at 56 hpf following heat-shock induction. Insets show 2D sections of the pillar or unfused buds from the regions in the white dashed boxes. Blue and yellow dashed lines indicate the anterior bud/pillar and the anterior-lateral bud/pillar, respectively. Scale bar: 50 µm. Representative images from two independent experiments are shown.

Extended movie 1: Mechanical epithelial cell recruitment during bud extension, related to Figure 4.

3D-rendered time-lapse images of the anterior bud obtained from *a Tg(actb2:membrane-neongreen-neongreen)* embryo. Each cell is marked by uniquely colored dot. Images were captured every 30 min. Time stamps indicate developmental time (hours post fertilization). Scale bar: 20 μm. Fig. 4b shows a cropped frame cropped from this movie.

Extended movie 2: Semicircular canal morphogenesis of wild-type embryo, related to Figure 5.

3D-rendered time-lapse images of the OV showing SCC formation of a wild-type embryo expressing membrane-NeonGreen. Images were captured every 30 min. Time stamps indicate developmental time (hours post fertilization). Scale bar: 50 μm.

Extended movie 3: Semicircular canal morphogenesis of *gpr126* $^{st49/st49}$ mutant embryo, related to Figure 5.

3D-rendered time-lapse images of the OV showing SCC formation of a *gpr126* $^{st49/st49}$ mutant embryo expressing membrane-NeonGreen. Images were captured every 30 min. Time stamps indicate developmental time (hours post fertilization). Scale bar: 50 μm.

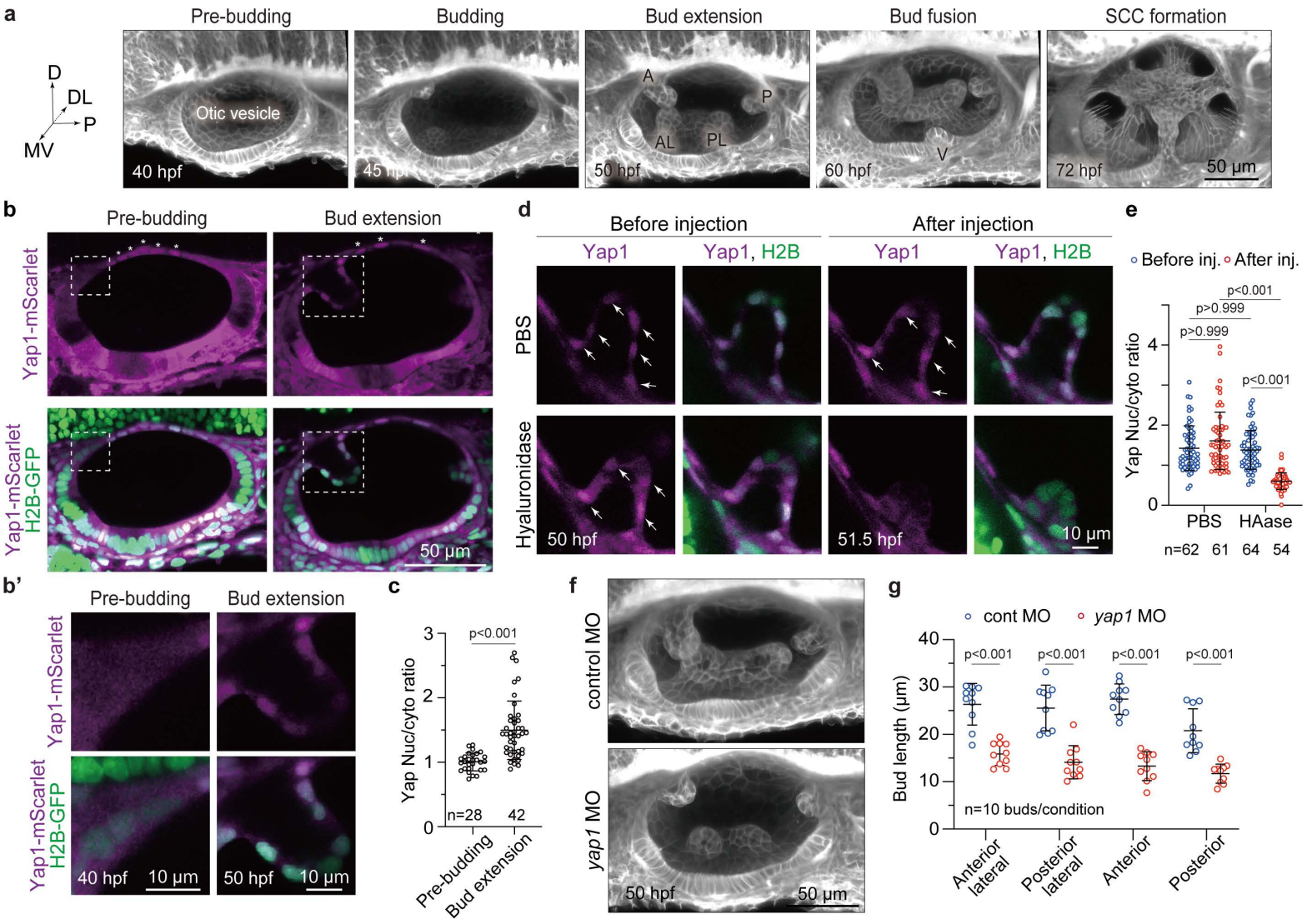

Fig 1, Mori et al.,

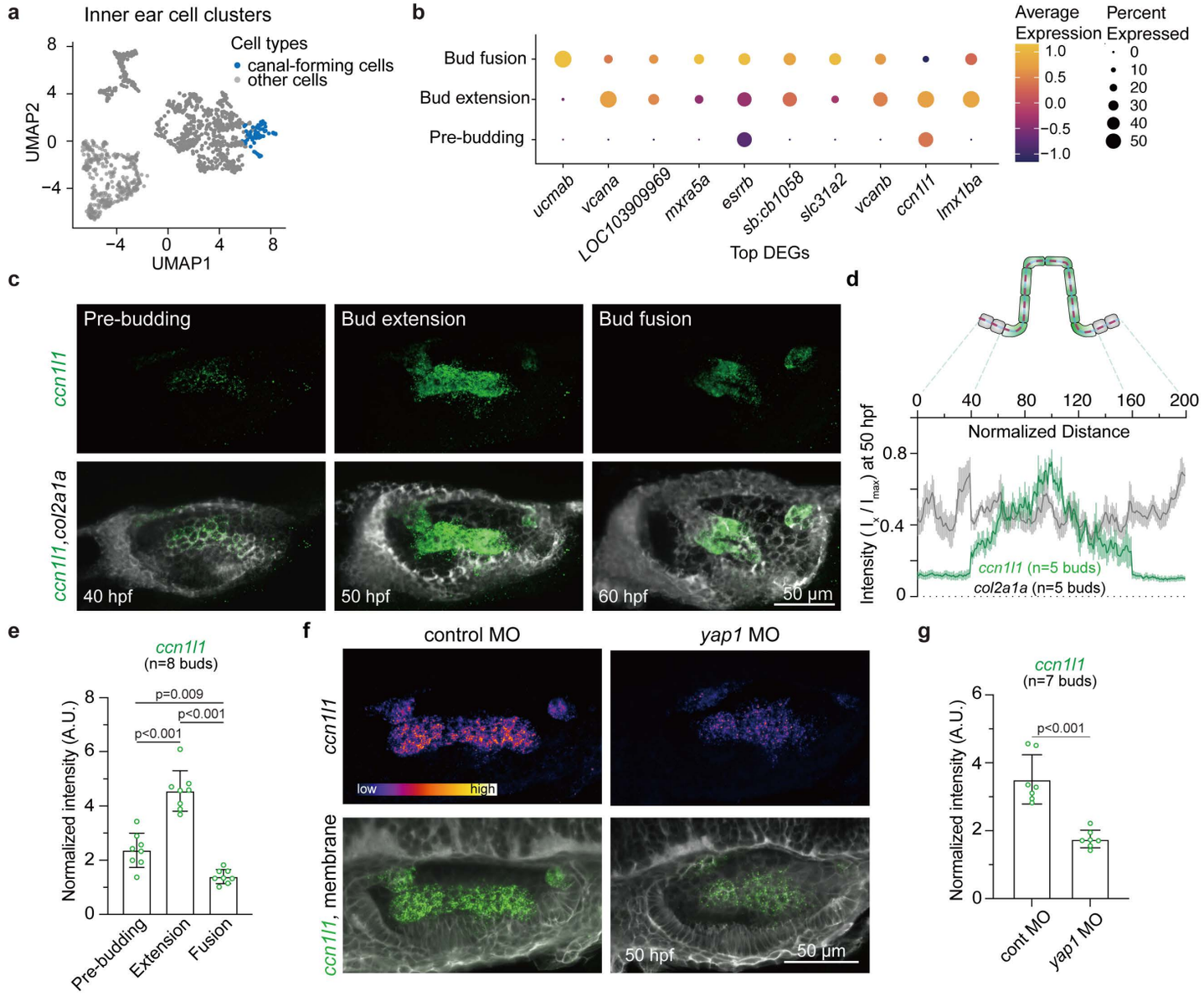

Fig 2, Mori et al.,

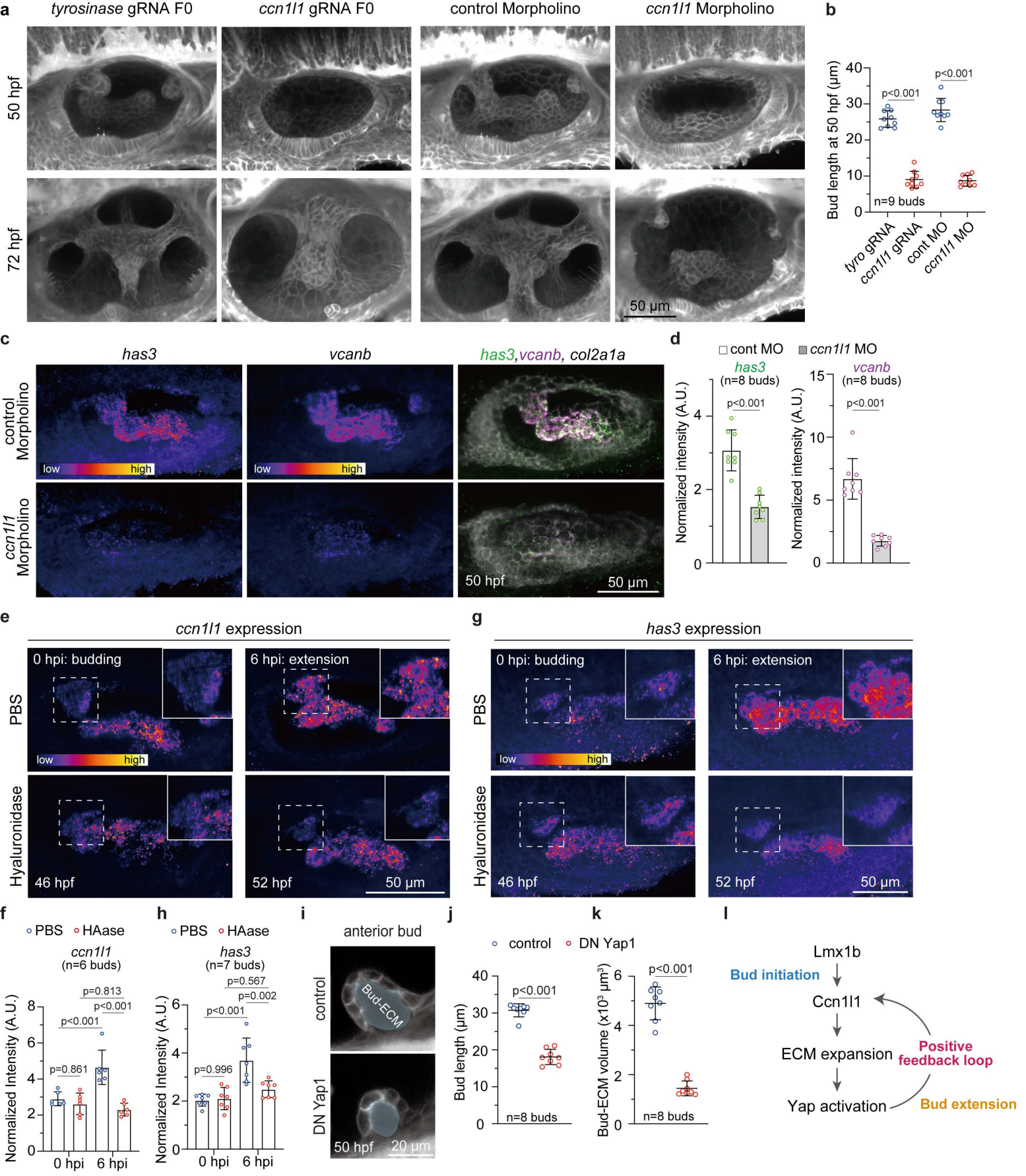

Fig 3, Mori et al.,

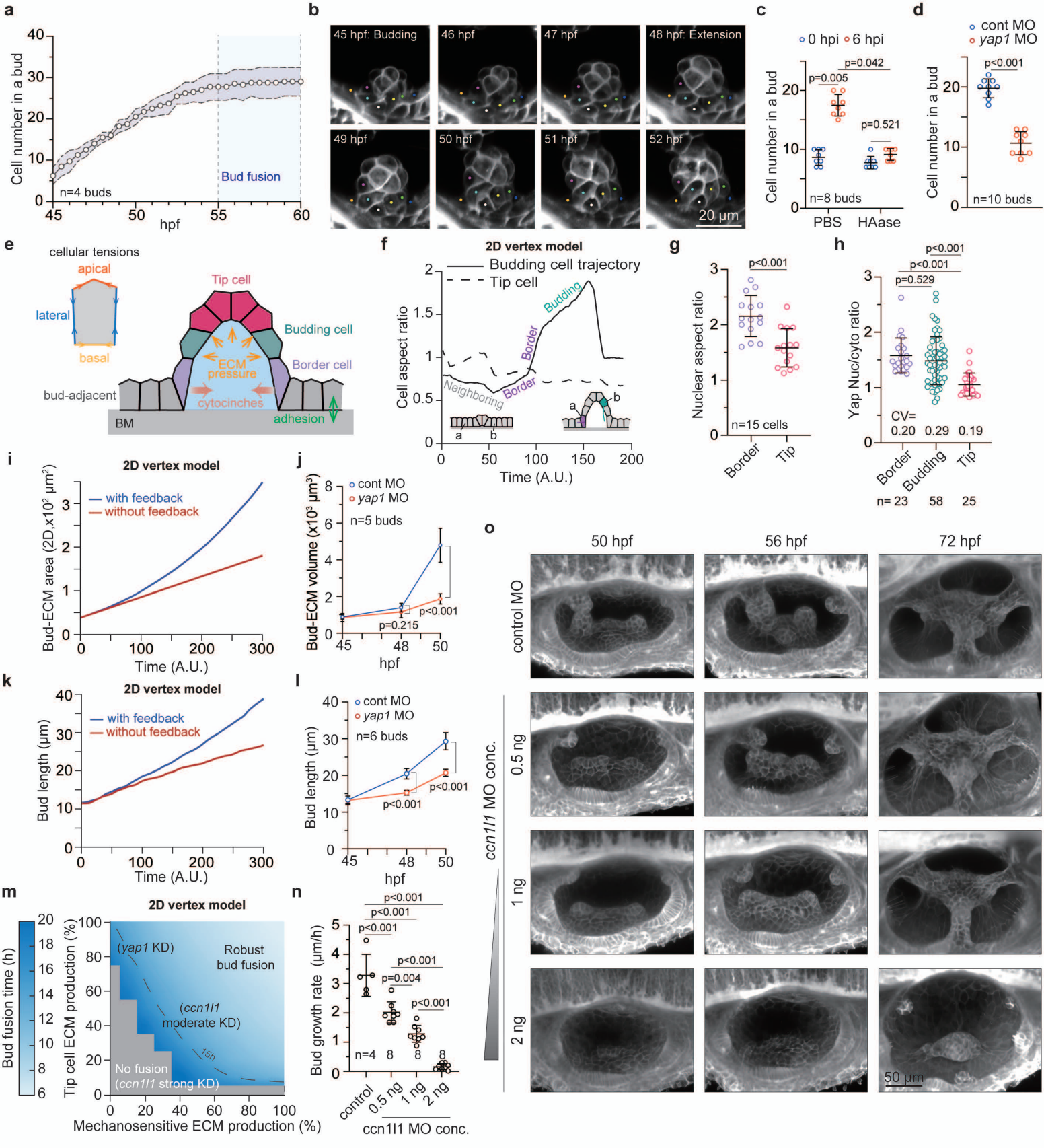

Fig 4, Mori et al.,

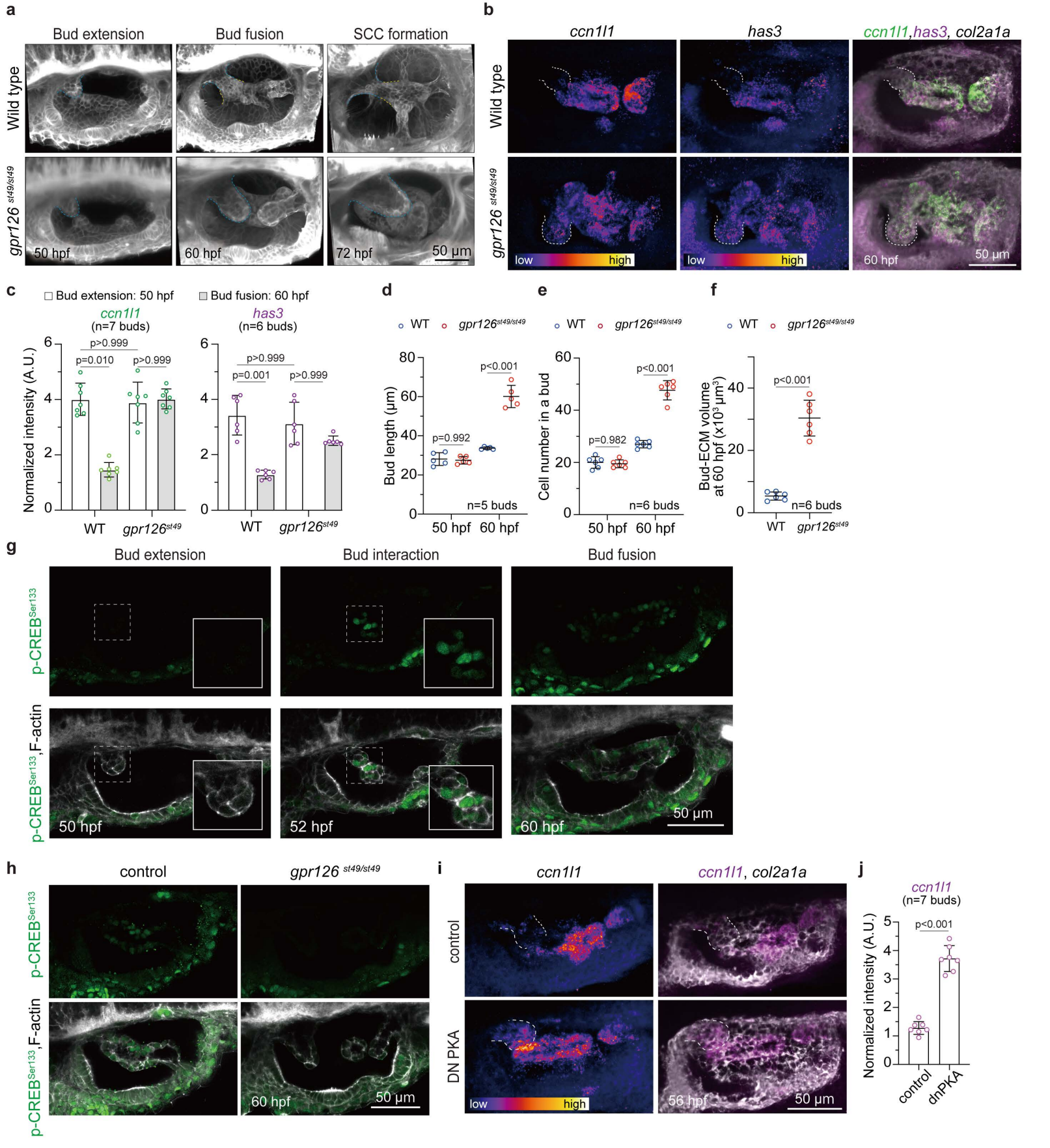

Fig 5, Mori et al.,

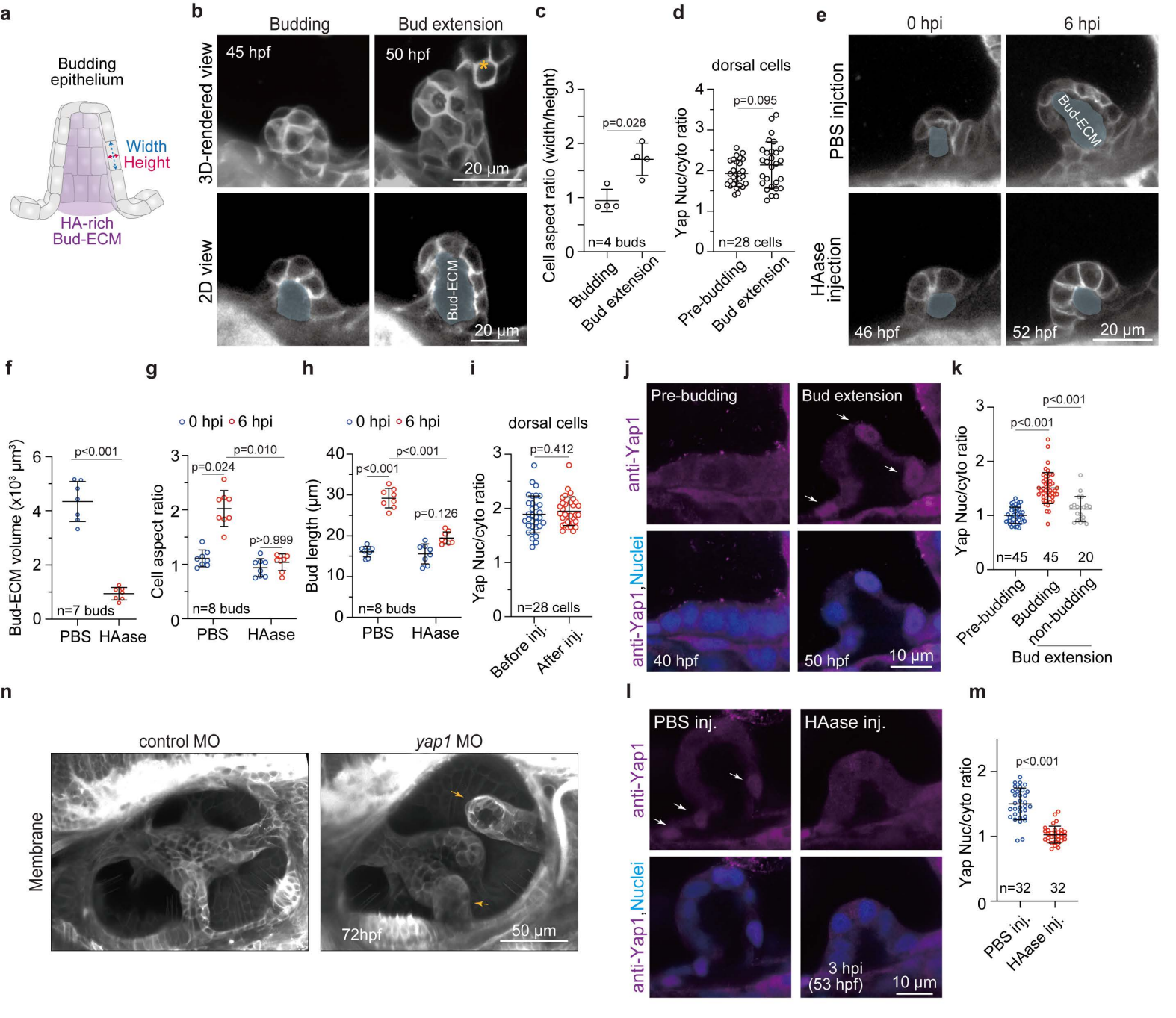

Extended Fig. 1, Mori et al.,

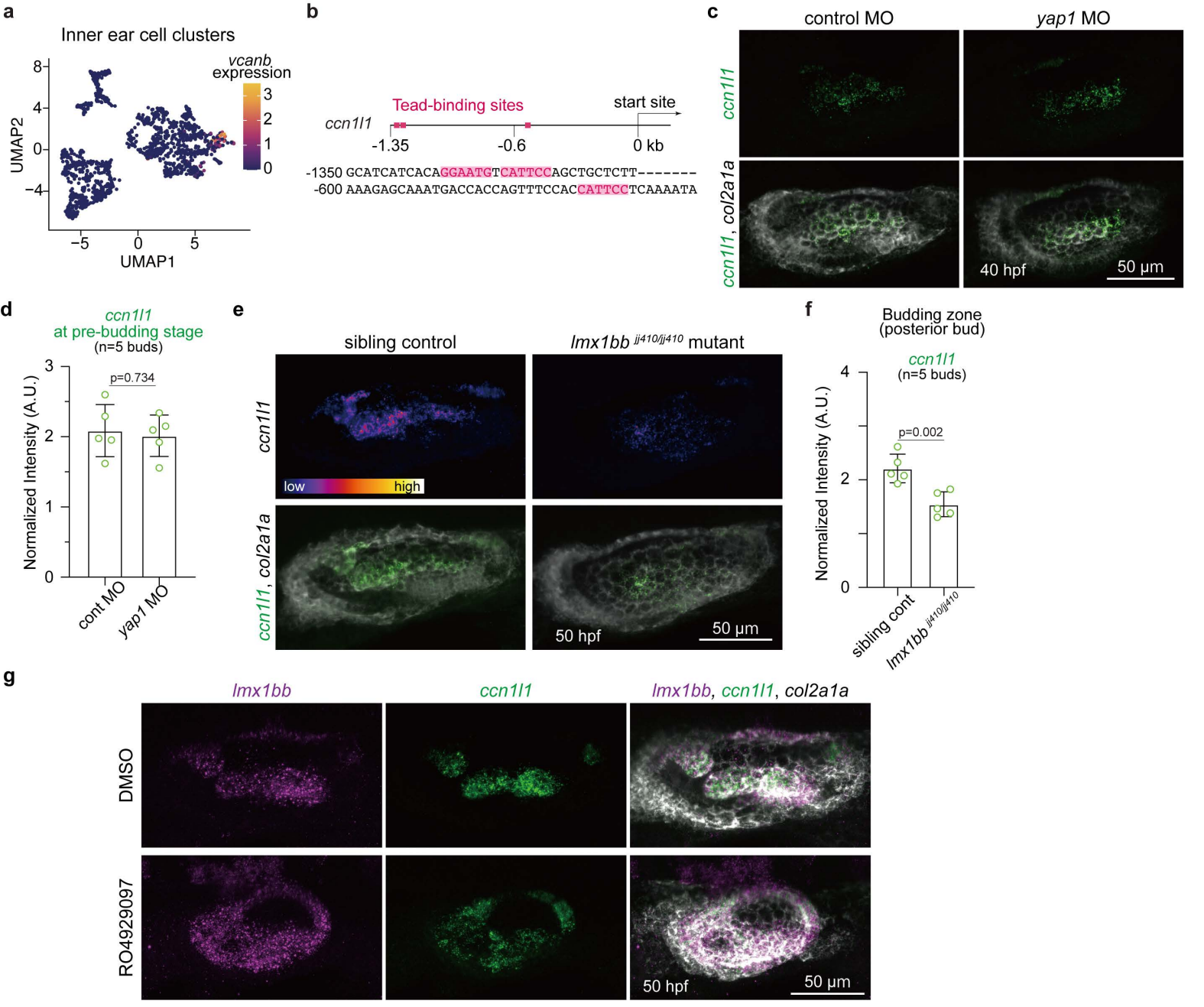

Extended Fig. 2, Mori et al.,

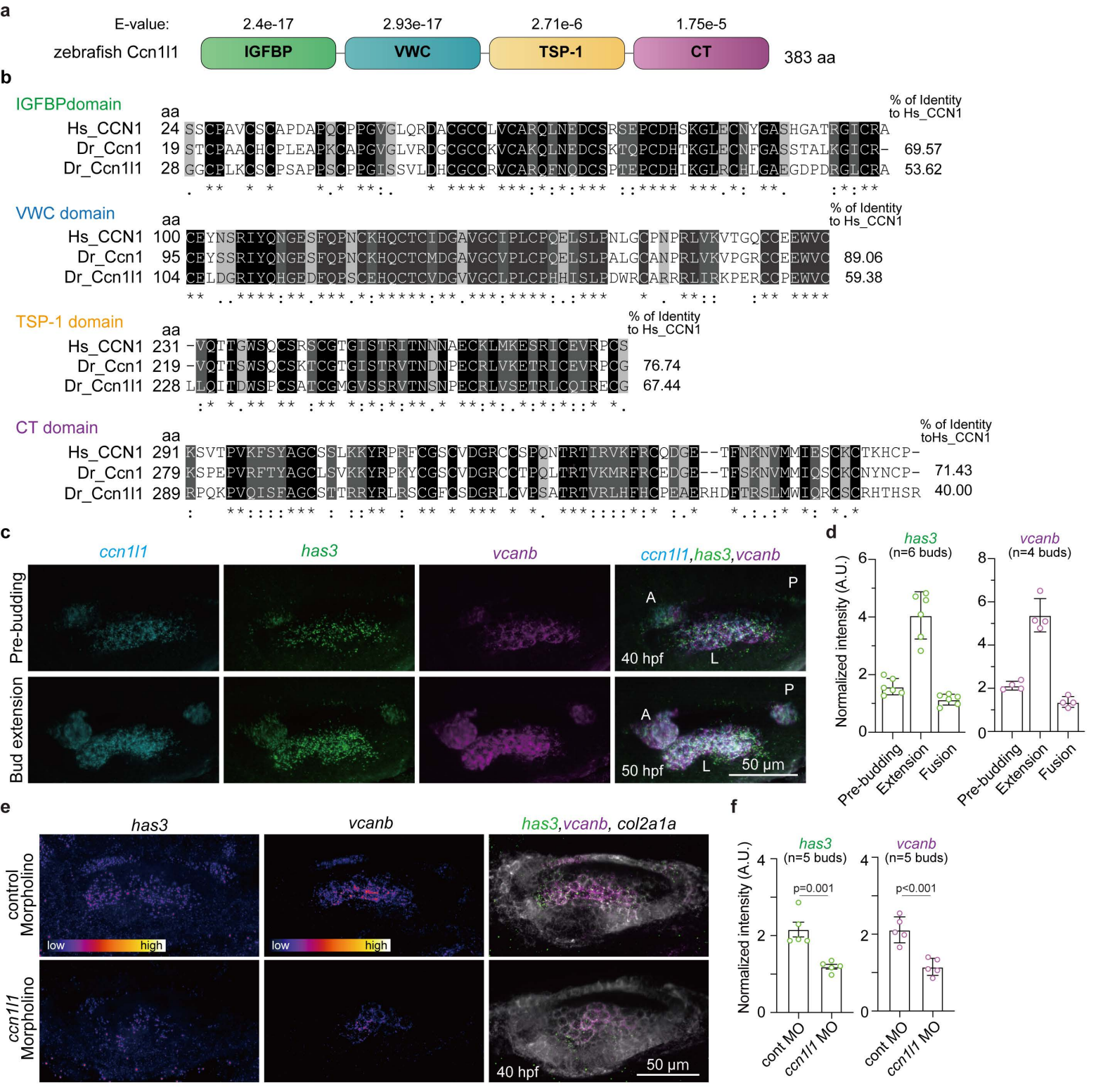

Extended Fig. 3, Mori et al.,

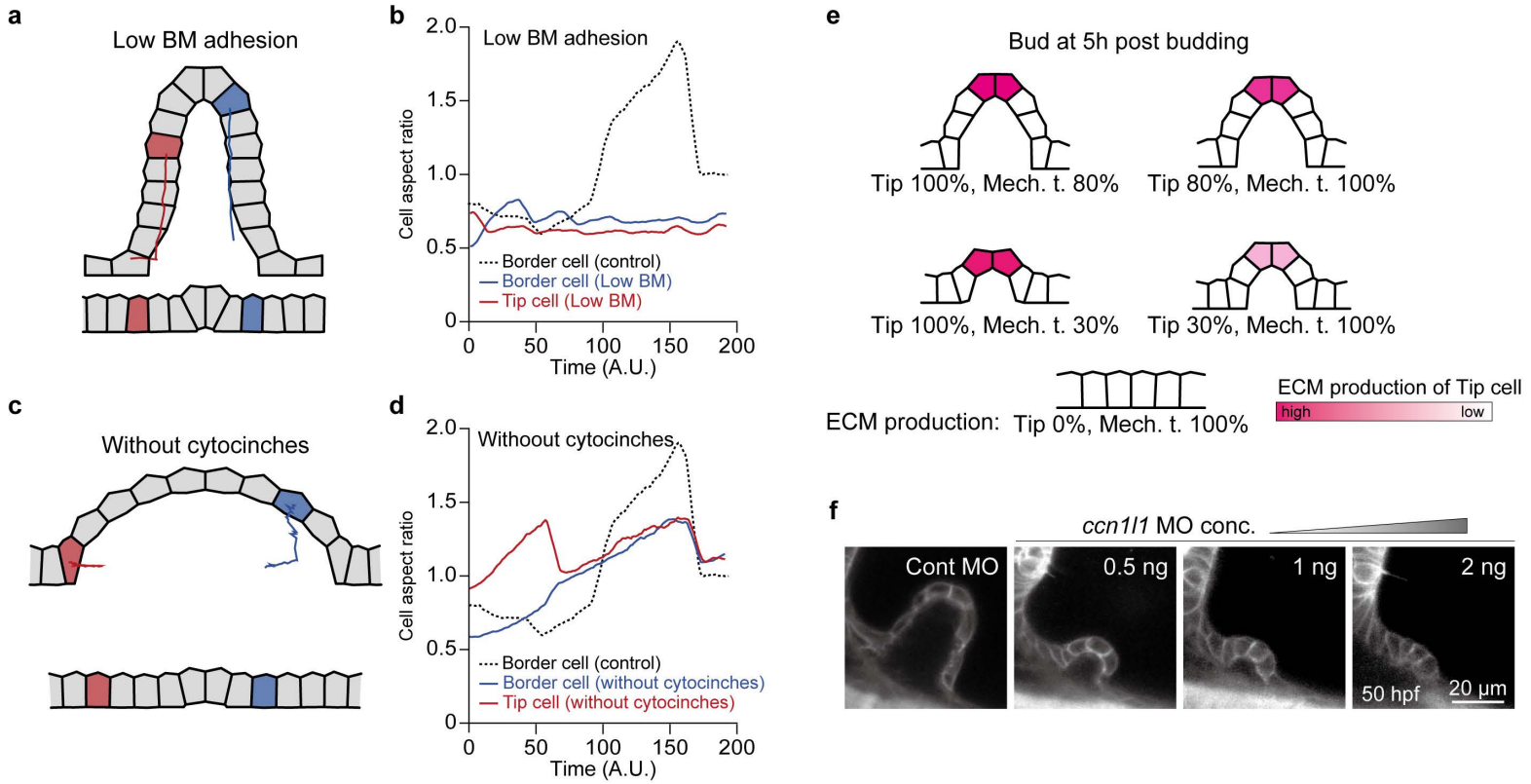

Extended Fig. 4, Mori et al.,

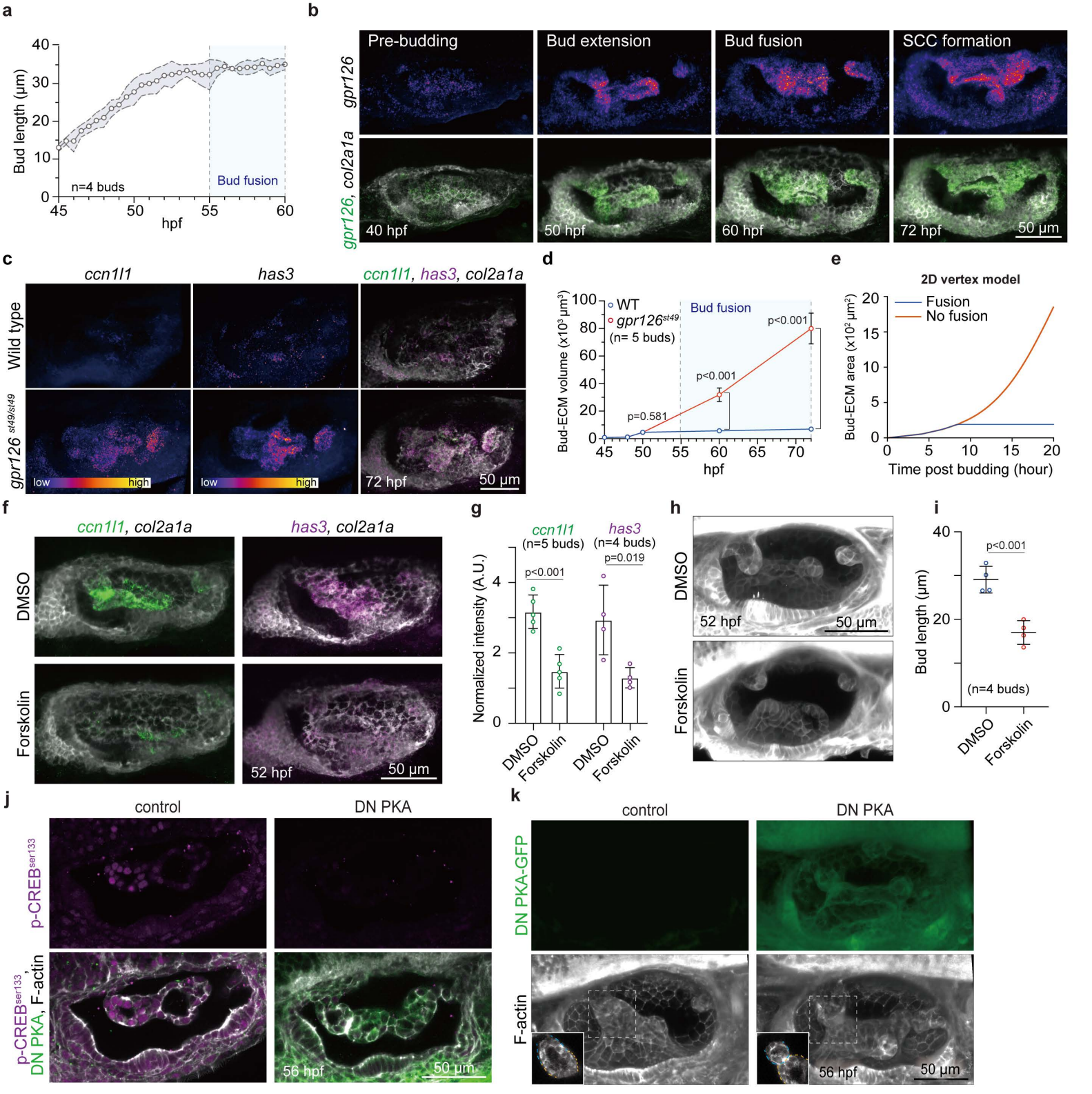

Extended Fig. 5, Mori et al.,

Supplementary Information – Theory note

In these notes, we detail the vertex models used to account for the bud morphogenesis, as well as analytical models to describe the role of the mechanotranduction feedback. These notes are organized as follows. In Section 1, we present the implementation of the vertex models. In Section 2, we focus on the elongation of budding cells during the recruitment process, in relation with YAP activation. In Section 3, we investigate the growth dynamics of the bud in presence of a feedback between YAP mechanotransduction and gel production.

1 Methods: Vertex model

1.1 Bud mechanics

As the bud is axisymmetric, we use here a 2D vertex model, representing a transversal cut across the bud in the xy plane. Because the radius of the bud is much smaller than the total size of the otic vesicle, we model the later as a planar surface at $y = 0$, from which the bud is growing. The system consists in N cells (corresponding to cells already recruited into the bud, and several rows of cells neighbouring the bud). The energy of a given cell i is taken to be:

$$e_i = (\gamma_a \ell_a + \gamma_b \ell_b + \gamma_l \ell_l) + K(a - a_0)^2 + \mathcal{U}_{\text{adh}} + \mathcal{U}_{\text{cytocinches}}, \tag{1}$$

where ℓ_a, ℓ_b and ℓ_l are the apical, basal and lateral lengths of the cell, respectively, and the γ's the respective mechanical tensions from the acto-myosin cytoskeleton. The second term imposes volume conservation, with a the 2D area of the cell, a_0 its homeostatis area and K a constant energy penalty for breaking volume conservation. To account for the corner-like shapes cells go through in vivo during the recruitment process, each cell is modelled by an hexagon, with 4 vertices corresponding to contact points with adjacent cells (2 on the apical side, and 2 on the basal side), and one additional vertex on both the apical and the basal sides, to allow cells to bend. The third term corresponds to an adhesion energy, for non-budded cells still in contact with the otic vesicle:

$$\mathcal{U}_{\text{adh}} = -G \times d_{\text{contact}} e^{-y/y_{\text{contact}}}, \tag{2}$$

where G is an adhesion energy per unit of contact length, d_{contact} is the portion of the cell's basal length that lies below some fixed threshold y_{contact}, and y is the average height of the cell's basal side. The exponential term allows for a smooth delamination of cells from the substrate, rather than a sharp threshold effect.

The last term in e_i accounts for cytocinches, actin-rich cables that were previously determined to constrict the bud and make it anisotropic, we applied a constricting force on all vertices that are part of the bud at a given timepoint (that is, that are not in contact with the horizontal substrate):

$$\mathcal{U}_{\text{cytocinches}} = \sum_{\text{basal vertex } j} k_c x_j^2, \tag{3}$$

where the sum runs other all the basal vertices of the cell, with x_j their horizontal position.

The total energy of the bud is then:

$$\mathcal{E} = K_{\text{ECM}}(A_{\text{ECM}} - A_0(t))^2 + \sum_{\text{cell } i=1}^{N} e_i, \tag{4}$$

where the first term imposes the volume of the ECM below the bud, with its equilibrium 2D area $A_0(t)$ being updated at each timestep to account for ECM production in the bud.

We then simulate the bud's mechanics through a Monte Carlo algorithm. At each timestep, we try optimizing the position and shape of each cell by randomly moving their vertices, and checking if the proposed change leads to a decrease in the total energy of the bud. In the initial state, cells on the horiizontal line are placed such that the epithelium is tension-free: each cell has a width $w = \sqrt{a \frac{\gamma_l}{\gamma_a + \gamma_b - G}}$ and height $h = a_0/w$, where a_0 is the homeostatic 2D area of a cell. The bud is assumed to have an axis of symmetry at its center, which in our simulation corresponds to the right-most vertices (the other half of the bud being obtained by axial symmetry). The position of the left-most vertex is kept constant throughout the simulation. All the codes were implemented in Julia.

1.2 Values of parameters

Cytoskeletal tensions can be estimated by considering cellular aspect ratios. At the start of the bud extension phase, when pressure from the ECM is still low, cells are likely close to their prefered aspect ratio, given by $\epsilon_0 = w_0/h_0 = \gamma_l/(\gamma_a + \gamma_b)$, with w_0 and h_0 the width and thickness of cells in their stress-free state. We measured that their thickness was approximately $h = 9\,\mu\text{m}$ and their width $w = 5\,\mu\text{m}$, resulting in an aspect ratio $\epsilon = w/h \simeq 0.55$. We chose γ_l, γ_a and $\gamma_b = 1$ to be all equal as this choice would yield $\epsilon_0 = 0.5$. In practice, experimental observations show that myosin is preferentially localized on the basal side; however, it is difficult to discriminate how much this basal myosin contributes directly to contraction, rather than simply to cell stiffness. In addition, cytocinches also contribute to contraction on the basal side. Therefore, we decided to keep $\gamma_b = \gamma_a = 1$ rather than considering more complex scenarios, and tuned basal contraction only through cytocinches.

We chose to work with length units so that the cell cross-section is $a_0 = 1$. Experimentally, the cell cross-section at the start of the bud extension phase was roughly $a_0 = 50\,\mu\text{m}^2$, so a unit length in our simulation corresponds to a distance $\sqrt{a_0} = 7\,\mu\text{m}$ in experiments.

The last two parameters, G and k_c, representing substrate adhesion and cytocinches contractility, respectively, cannot be directly determined experimentally. Intuitively, the corresponding forces must be of the same order as the in-plane tissue tension $\gamma_a + \gamma_b$, and their precise values could be obtained by fitting the length and radius of the bud for different parameter values on experimental data. However, the 2D and highly simplified nature of our model makes such a fitting procedure rather questionable. Instead, we chose to set $G = 0.5$ and $k_c = 0.2$ in most cases, and we tested the impact of changing these values on the bud morphology.

In the following, we considered two separate cases for the dynamics of the ECM production, defined by $A_0(t)$. As a first step, we externally prescribed A_0 to slowly increase at a constant rate, to focus on cell recruitment alone. Then, we considered the role of the mechanotransduction feedback, and assume that the growth rate $\dot{A}_0$ was proportional to the number of recruited cells.

When testing the effects of a low adhesion, we set $G = 0.3$. In simulations without cytocinches, we set $k_c = 0.0$.

2 Cell elongation during the recruitment process

2.1 Link between cellular aspect ratio and mechanical forces

At the lowest possible degree of description, apical, basal and lateral cytoskeletal tensions create a spring-like restoring force, causing each cell to spontaneously return to a prefered aspect ratio. For a rectangular 2D cell, this prefered value can be determined as:

$$\epsilon_0 = \frac{w_0}{h_0} = \frac{w_0^2}{a_0} = \frac{\gamma_l}{\gamma_a + \gamma_b}, \tag{5}$$

where ϵ_0 is the prefered aspect ratio, w_0 the prefered width, h_0 the height of the cell, a_0 its 2D cross-section, and γ_l, γ_a, γ_b are the lateral, apical and basal tensions. As a result, a deformed cell, with aspect ratio $\epsilon > \epsilon_0$ will exert a pulling force on its environment, given by:

$$\zeta = \gamma_a + \gamma_b - \gamma_l \epsilon^{-1} \simeq (\gamma_a + \gamma_b)\frac{w - w_0}{w_0}, \tag{6}$$

so that this pulling force is proportional to the relative elongation of the cell. Therefore, in what follows, we monitor the aspect ratio $\epsilon = \frac{w^2}{a}$ as a readout of mechanical forces felt by the cells. When $\epsilon > \epsilon_0$, the cell is under stretch, and this can typically result in nuclear relocalization of Yap.

2.2 Cell aspect ratio during recruitment

Based on this result, we monitor the cellular aspect ratio of all cells in our simulations. First, we assume that bud ECM production is prescribed independently from cell recruitment, and we impose that $A_0 = rt$, with r a constant growth rate. As cells are not rectangular, we define numerically w as the average of the apical and basal sides of the cell, and compute the aspect ratio through $\epsilon = w^2/a_0$. While other definitions of the aspect ratio are possible, this one directly relates to mechanical forces as it results from the balance between apical, basal, and lateral tensions with external forces from the surrounding tissue.

Numerically, we find that cells undergo a transient stretching as they are recruited into the bud: border cells, that are partially recruited and partially still attached to the basement membrane exhibit an overshoot in their aspect ratio, and similarly for budding cells (bud cells that are adjacent to a border cell). On the other hand, tip cells showed a lower aspect ratio. Looking at trajectories of individual cells, we find that they "flow" towards the bud, and start stretching as they turn the corner. Bud adjacent cells (cells neighboring border cells, but still attached to the basement membrane) displayed a slight compression. Intuitively, we would expect that the flow of cells converging around the bud would result in an in-plane tension that decreases with distance from the bud, resulting instead to a slight stretching of bud adjacent

cells. However, our 2D simulation does not model the fluidity (through in-plane rearrangements and friction with the substrate) of the epithelium around the bud. Therefore, we assume that this slight compression of bud adjacent cell stems from a small simulation artefact.

We hypothesized that the increase in aspect ratio of border cells was the result of a tug-of-war between adhesion forces, which pull the epithelium towards the basement membrane, and tugging forces from the cytocinches. To test this idea, we considered the effects of either reducing focal adhesion, or removing forces from cytocinches. The former led to over-recruitment of cells. The latter, on the other hand, fully suppressed the converging flow of cells towards the bud. Instead, the bud appeared to radially "push" the epithelium away from the center. In both cases, the aspect ratio of cells remained low and no marked difference was found between border cells and tip cells.

3 Role of the feedback loop

Next, we consider the impact of this mechanical patterning on the bud extension dynamics. Rather than prescribing the volume increase of the bud ECM, we now assume its rate depends on the number of recruited cells. We consider the following model:

$$\frac{\mathrm{d}A_{\mathrm{ECM}}}{\mathrm{d}t} = k(aN_{\mathrm{tip}} + bN_{\mathrm{recruited}}), \tag{7}$$

where bud ECM production is the sum of two contributions: a constant rate from tip cells, and a variable contribution from recruited cells that grows as the bud recruits more and more cells. Setting $b = 0$ allows us to mimick Yap morpholino conditions, while $b = a = 1$ would be closer to wild type conditions. Here, the quantity k is a unit of ECM volume production per unit of time, setting the unit of time of our simulation. Here we choose $k = 13\,\mu\mathrm{m}^3/\mathrm{h}$, with one hour corresponding to 30000 simulation steps.

Numerically, we find that the mechanical feedback increases the bud extension rate, as well as the cell recruitment rate. The tell-sign of the feedback is the growth dynamics of the bud-ECM volume A_{ECM}: in absence of any feedback, it grows linearly and slowly, while in its presence it grows supra-linearly. This observation is fully in line with experimental findings. In particular, in the gpr126 mutant, the bud ECM volume displays a clear non linear growth as the feedback continues unimpeded in absence of bud fusion.

To study the impact of the feedback loop on bud fusion, we define bud fusion as the moment when the bud reaches 30 µm in length. The start of our simulation corresponds roughly to a timepoint of 50 hpf. If the bud does not reach this value after 22 hours (72 hpf), we assume that the bud fails to fuse.

Extended Table 1

Target gene	amplifier type	Probe Name	Sequence
ccn1l1	B3	ccn1l1_B3_1	TTTTTTTTTTTTTTTTTTTTTTTTTTTTCCACTCAACTTTAACCCG
ccn1l1	B3	ccn1l1_B3_2	GTCCCTGCCTCTATATCTTTGGAAATTGTAACACATTTTTATTTG
ccn1l1	B3	ccn1l1_B3_3	ATTCACCTCAAAAAATTGAGGTTTGTTCCACTCAACTTTAACCCG
ccn1l1	B3	ccn1l1_B3_4	GTCCCTGCCTCTATATCTTTTATGACTCTTCACAAGAACTGAAGA
ccn1l1	B3	ccn1l1_B3_5	ATATTTACAGCGATATTTGTACAAATTCCACTCAACTTTAACCCG
ccn1l1	B3	ccn1l1_B3_6	GTCCCTGCCTCTATATCTTTTACACTATATACAGTAAATCTGGAT
ccn1l1	B3	ccn1l1_B3_7	GTGTGTGTAAATTATATAAACCAAATTCCACTCAACTTTAACCCG
ccn1l1	B3	ccn1l1_B3_8	GTCCCTGCCTCTATATCTTTAGCTTTGCAGTCATACCGTAATAAA
ccn1l1	B3	ccn1l1_B3_9	TCTTCCACCTGTGTCATTACCACATTTCCACTCAACTTTAACCCG
ccn1l1	B3	ccn1l1_B3_10	GTCCCTGCCTCTATATCTTTATAATAAAACGGTAATATTTAAAAC
ccn1l1	B3	ccn1l1_B3_11	TATGCTGGGTTTAAATGTTTTGTAGTTCCACTCAACTTTAACCCG
ccn1l1	B3	ccn1l1_B3_12	GTCCCTGCCTCTATATCTTTTGAGGGCAGTGTGGATCTGTTGCTG
ccn1l1	B3	ccn1l1_B3_13	TCAGCTGGTGTGTTCAGGCCTCGTCTTCCACTCAACTTTAACCCG
ccn1l1	B3	ccn1l1_B3_14	GTCCCTGCCTCTATATCTTTCTGTGTGTGTGTCTGCAGCTGCAGC
ccn1l1	B3	ccn1l1_B3_15	CTCTGGACAGTGGAAATGCAGACGGTTCCACTCAACTTTAACCCG
ccn1l1	B3	ccn1l1_B3_16	GTCCCTGCCTCTATATCTTTTGTCCGAGTTGCAGATGGGACACAC
ccn1l1	B3	ccn1l1_B3_17	GGCGAGTAGTGGAACATCCAGCAAATTCCACTCAACTTTAACCCG
ccn1l1	B3	ccn1l1_B3_18	GTCCCTGCCTCTATATCTTTTGATCTGCACAGGTTTCTGTGGCCG
ccn1l1	B3	ccn1l1_B3_19	GTGTTGACGCCACACTCTCGGATCTTTCCACTCAACTTTAACCCG
ccn1l1	B3	ccn1l1_B3_20	GTCCCTGCCTCTATATCTTTCAGAGTCTGGTTTCGCTTACTAGCC
ccn1l1	B3	ccn1l1_B3_21	TCCACAGGTGGCAGAGCATGGCGACTTCCACTCAACTTTAACCCG
ccn1l1	B3	ccn1l1_B3_22	GTCCCTGCCTCTATATCTTTATCGGTGATCTGCAGCAAGCAGGTG
ccn1l1	B3	ccn1l1_B3_23	GATAAGGGGCTCCTGCACTGCTGTCTTCCACTCAACTTTAACCCG
ccn1l1	B3	ccn1l1_B3_24	GTCCCTGCCTCTATATCTTTAGGAAGCAGATGGAGTTACCAGTAG
ccn1l1	B3	ccn1l1_B3_25	GGCACTGGATTCACCTCAGCAATGCTTCCACTCAACTTTAACCCG
ccn1l1	B3	ccn1l1_B3_26	GTCCCTGCCTCTATATCTTTTTGTCGTCATCACAGACCCACTCCG
ccn1l1	B3	ccn1l1_B3_27	GCGCCAGTCGGGCAGAGAGATGTGGTTCCACTCAACTTTAACCCG
ccn1l1	B3	ccn1l1_B3_28	GTCCCTGCCTCTATATCTTTTGGGCACAGTGGCAGACAGCCGACC
ccn1l1	B3	ccn1l1_B3_29	AGTCCTCTCCGTGCTGGTAAATCCGTTCCACTCAACTTTAACCCG
ccn1l1	B3	ccn1l1_B3_30	GTCCCTGCCTCTATATCTTTCATCCAGCTCACACGGGCGACCCTG
ccn1l1	B3	ccn1l1_B3_31	CCTAGGTGGCAGCGCAGTCCTTTAATTCCACTCAACTTTAACCCG
ccn1l1	B3	ccn1l1_B3_32	GTCCCTGCCTCTATATCTTTTGGTCGCAGGGTTCAGTAGGGCTGC
ccn1l1	B3	ccn1l1_B3_33	GTGGTCCAAAACCGAGCTGATACCTTTCCACTCAACTTTAACCCG
ccn1l1	B3	ccn1l1_B3_34	GTCCCTGCCTCTATATCTTTAGGACACGAGGGGGGAGCGGAAGGA
ccn1l1	B3	ccn1l1_B3_35	CCCATGACAGCAGCACCAGTGTGAATTCCACTCAACTTTAACCCG
ccn1l1	B3	ccn1l1_B3_36	GTCCCTGCCTCTATATCTTTAATGTCCTTGCCTTAATATGATCCT

ccn1l1	B3	ccn1l1_B3_37	CAGAAAGTGTCTTCTGGTTTAGACCTTCCACTCAACTTTAACCCG
ccn1l1	B3	ccn1l1_B3_38	GTCCCTGCCTCTATATCTTTGTTCTGGATCTGTCAATTCACAAGG
ccn1l1	B3	ccn1l1_B3_39	TGGCTAAATGCAAAAAACTGCAAAGTTCCACTCAACTTTAACCCG
ccn1l1	B3	ccn1l1_B3_40	GTCCCTGCCTCTATATCTTTGTGTGCTGCTGGATTCCCTCAGTGA
has3	B2	has3_B2_1	TCAGATAAGCCCCGACAGCATTTAGAAATCATCCAGTAAACCGCC
has3	B2	has3_B2_2	CCTCGTAAATCCTCATCAAAAGCATATAAACCATGCTAGGCTTCG
has3	B2	has3_B2_3	ACGTTTGGCCACTATGGCCAGGTAGAAATCATCCAGTAAACCGCC
has3	B2	has3_B2_4	CCTCGTAAATCCTCATCAAACACCAGGAGTATAAGCCAGTAAGAG
has3	B2	has3_B2_5	AGTCTCGGTAAAAGGTTCTTGAACCAAATCATCCAGTAAACCGCC
has3	B2	has3_B2_6	CCTCGTAAATCCTCATCAAAGCAGTAAATGGTGTAAACCACTCCA
has3	B2	has3_B2_7	TCCAATAAGGTTTACTACCATCTTTAAATCATCCAGTAAACCGCC
has3	B2	has3_B2_8	CCTCGTAAATCCTCATCAAACCTGCCTGATGTGCCCCATCCTGCT
has3	B2	has3_B2_9	CAGGCTTGACATGTAGAGCAGTGAGAAATCATCCAGTAAACCGCC
has3	B2	has3_B2_10	CCTCGTAAATCCTCATCAAAGAGTGACATGAAGATCATGACAAGG
has3	B2	has3_B2_11	ACCCACCAGCTGGACCGTCAACAAGAAATCATCCAGTAAACCGCC
has3	B2	has3_B2_12	CCTCGTAAATCCTCATCAAAGAGTAAGATGTTCCACAACCGGCCT
has3	B2	has3_B2_13	GGGGAAGAACCCAGTAACCACAGATAAATCATCCAGTAAACCGCC
has3	B2	has3_B2_14	CCTCGTAAATCCTCATCAAAATAGGTCATCCACAGGCTGTGCTTG
has3	B2	has3_B2_15	AGACTTGCTCCAGCGGGTCTGCTGAAAATCATCCAGTAAACCGCC
has3	B2	has3_B2_16	CCTCGTAAATCCTCATCAAAGAGCCAACGCAGGTATTGTGTTGGG
has3	B2	has3_B2_17	TTTGAAGCCAAAGCTAAGGACGCGGAAATCATCCAGTAAACCGCC
has3	B2	has3_B2_18	CCTCGTAAATCCTCATCAAAGGTGAGATGTCGATCATCACCAAAA
has3	B2	has3_B2_19	CTCTAAGAACTGCTGAAGGAGAGAGAAATCATCCAGTAAACCGCC
has3	B2	has3_B2_20	CCTCGTAAATCCTCATCAAAACGGTACATTCCTAGAGGTCCACTG
has3	B2	has3_B2_21	CTCCACATTGAAGGCCATCCAATAGAAATCATCCAGTAAACCGCC
has3	B2	has3_B2_22	CCTCGTAAATCCTCATCAAAGACACTGCTCAGGAAGGAGATCCAG
has3	B2	has3_B2_23	TCCTCCCACATCAGGATCCTCCTCTAAATCATCCAGTAAACCGCC
has3	B2	has3_B2_24	CCTCGTAAATCCTCATCAAAAATCTTCAACATCTCAATAGTGCAT
has3	B2	has3_B2_25	GTAATCCACTGTATCTCCAAGTGCTAAATCATCCAGTAAACCGCC
has3	B2	has3_B2_26	CCTCGTAAATCCTCATCAAAGAAGGCTGTATACATCACTTCCCTC
has3	B2	has3_B2_27	GCTCCGCACCACTCTGGCCACTCGTAAATCATCCAGTAAACCGCC
has3	B2	has3_B2_28	CCTCGTAAATCCTCATCAAAAGCCTCTTCGGCATGCACCGAGCCT
has3	B2	has3_B2_29	ATTCCCTTTCCACACCACACAGCCTAAATCATCCAGTAAACCGCC
has3	B2	has3_B2_30	CCTCGTAAATCCTCATCAAACTGCTCCACTCCCCCCATCACCTCC
has3	B2	has3_B2_31	GCCATCCACCACCAACACCACTTTCAAATCATCCAGTAAACCGCC
has3	B2	has3_B2_32	CCTCGTAAATCCTCATCAAACCCGGGAAAAGAAATGCGGCGAATG
has3	B2	has3_B2_33	ATAGGCTGCAATGCAGAGGGCCACAAAATCATCCAGTAAACCGCC
has3	B2	has3_B2_34	CCTCGTAAATCCTCATCAAAGCGGCGCAGGTGCTGCGGTCTGGAG
has3	B2	has3_B2_35	ACTCTGCAGGAGAAGGTGGAGGGATAAATCATCCAGTAAACCGCC

has3	B2	has3_B2_36	CCTCGTAAATCCTCATCAAAAAATGCACCGTACAAGCCAAAAGAC
has3	B2	has3_B2_37	CACATAGGCTAGTAGGATTGCGAAAAAATCATCCAGTAAACCGCC
has3	B2	has3_B2_38	CCTCGTAAATCCTCATCAAACACCACTGCTGCAAATAAGGTGGTG
has3	B2	has3_B2_39	CTGAAGAAGGAAAAAAACATGACTTAAATCATCCAGTAAACCGCC
has3	B2	has3_B2_40	CCTCGTAAATCCTCATCAAAGTGTAGAAAGCAAAATCATTACTGC
lmx1bb	B2	lmx1bb_B2_1	TAGGCTCAGTGGCTAGCATTGTCGCAAATCATCCAGTAAACCGCC
lmx1bb	B2	lmx1bb_B2_2	CCTCGTAAATCCTCATCAAACACTGCAGCTATATATATTTATTTA
lmx1bb	B2	lmx1bb_B2_3	TAATTTTGGTTTCTTCATGTAGCAAAAATCATCCAGTAAACCGCC
lmx1bb	B2	lmx1bb_B2_4	CCTCGTAAATCCTCATCAAAGTTTAAGTTTTCCTAATGCATGTTC
lmx1bb	B2	lmx1bb_B2_5	CTTTATTGCATGCAGATTCATTTCAAAATCATCCAGTAAACCGCC
lmx1bb	B2	lmx1bb_B2_6	CCTCGTAAATCCTCATCAAATTTGTTTCCGTGGATGCCAGGCAAA
lmx1bb	B2	lmx1bb_B2_7	ACGGAAGTTACTTAAGTTTATTGAAAAATCATCCAGTAAACCGCC
lmx1bb	B2	lmx1bb_B2_8	CCTCGTAAATCCTCATCAAATTATCTACTTAATATTCTAATCATC
lmx1bb	B2	lmx1bb_B2_9	TCAAATGCTTCCATCTGACAAGCACAAATCATCCAGTAAACCGCC
lmx1bb	B2	lmx1bb_B2_10	CCTCGTAAATCCTCATCAAAGTCTATACAGTCGAAGCTCTCCAAA
lmx1bb	B2	lmx1bb_B2_11	CCATGTGCCACCAACAACCATGCCAAAATCATCCAGTAAACCGCC
lmx1bb	B2	lmx1bb_B2_12	CCTCGTAAATCCTCATCAAATTCAAAGTTACTTAAATCACCTTTA
lmx1bb	B2	lmx1bb_B2_13	TGTTTGGCATTTTAGTGGCGCTCAAAAATCATCCAGTAAACCGCC
lmx1bb	B2	lmx1bb_B2_14	CCTCGTAAATCCTCATCAAAGGCGAAGCAAATTCGATTTCTGCTC
lmx1bb	B2	lmx1bb_B2_15	ATCACTTTGCTTTTACTATATGTGTAAATCATCCAGTAAACCGCC
lmx1bb	B2	lmx1bb_B2_16	CCTCGTAAATCCTCATCAAACTTTCCTAGCTTTCGGGTCTAGTCT
lmx1bb	B2	lmx1bb_B2_17	ACAGAACTGAACAGATTGAAACAAAAAATCATCCAGTAAACCGCC
lmx1bb	B2	lmx1bb_B2_18	CCTCGTAAATCCTCATCAAAAAACAGAACAGAATCGATTGAAACA
lmx1bb	B2	lmx1bb_B2_19	GCATTTTTCCAATAAAATCTCTCCAAAATCATCCAGTAAACCGCC
lmx1bb	B2	lmx1bb_B2_20	CCTCGTAAATCCTCATCAAATCCTTCAGATTCTCTAGTCCATGTT
lmx1bb	B2	lmx1bb_B2_21	TTTGTTTTTCCTTTTAAATAGCATGAAATCATCCAGTAAACCGCC
lmx1bb	B2	lmx1bb_B2_22	CCTCGTAAATCCTCATCAAAGGTTATAAAATAGCATTTTAGGTTA
lmx1bb	B2	lmx1bb_B2_23	ATCCCGCTTTTGCATATTTGCAGAGAAATCATCCAGTAAACCGCC
lmx1bb	B2	lmx1bb_B2_24	CCTCGTAAATCCTCATCAAACTCGCTTCAGAACACCTTATATTAC
lmx1bb	B2	lmx1bb_B2_25	GGTGTGACCAGCTGTCGCCATTTAGAAATCATCCAGTAAACCGCC
lmx1bb	B2	lmx1bb_B2_26	CCTCGTAAATCCTCATCAAACGCACGCCATCACGCCGACCAGGGG
lmx1bb	B2	lmx1bb_B2_27	TCAGTGTATTCAGATTAGTTGTGTTAAATCATCCAGTAAACCGCC
lmx1bb	B2	lmx1bb_B2_28	CCTCGTAAATCCTCATCAAAAAGTTTAATCAGTCACTCTACCTAG
lmx1bb	B2	lmx1bb_B2_29	GTCTGACCTTTAAAAAAAGAATAAAAAATCATCCAGTAAACCGCC
lmx1bb	B2	lmx1bb_B2_30	CCTCGTAAATCCTCATCAAAATCATCTCAGTGAATCTCTTCACAT
lmx1bb	B2	lmx1bb_B2_31	TCCAGCCGCAGCCCATTTCTGGGAAAAATCATCCAGTAAACCGCC
lmx1bb	B2	lmx1bb_B2_32	CCTCGTAAATCCTCATCAAAATCCACACACACATTCACACACACA
lmx1bb	B2	lmx1bb_B2_33	TCATATAATTTAGTACCATTTGCTCAAATCATCCAGTAAACCGCC
lmx1bb	B2	lmx1bb_B2_34	CCTCGTAAATCCTCATCAAACACCCAATGACGGTTGGGTTTAGGG

lmx1bb	B2	lmx1bb_B2_35	ATCTGTTATAAACGCACCACTGAACAAATCATCCAGTAAACCGCC
lmx1bb	B2	lmx1bb_B2_36	CCTCGTAAATCCTCATCAAATGGGAAGTTTTTTGTTTGTTATGAG
lmx1bb	B2	lmx1bb_B2_37	TTGGTTGCCAATAAGCTTGTTCCTCAAATCATCCAGTAAACCGCC
lmx1bb	B2	lmx1bb_B2_38	CCTCGTAAATCCTCATCAAACATTTAAATACCTCAGTGTTGTAGC
lmx1bb	B2	lmx1bb_B2_39	TTGCAATTTAATCAATAAATAATTTAAATCATCCAGTAAACCGCC
lmx1bb	B2	lmx1bb_B2_40	CCTCGTAAATCCTCATCAAATTATTTATTAATTAGTCTGTTACTT
vcanb	B1	vcanb_B1_1	TTTTTTTTTTTTTTTTTTTTTTTTTTTAGAAGAGTCTTCCTTTACG
vcanb	B1	vcanb_B1_2	GAGGAGGGCAGCAAACGGAATTAATATTCTAATAGCGCTTTATTA
vcanb	B1	vcanb_B1_3	TATATTTTGATGAGCATATGATTGTTAGAAGAGTCTTCCTTTACG
vcanb	B1	vcanb_B1_4	GAGGAGGGCAGCAAACGGAAGAGTGTACAATGGCGTTCTCTGAAG
vcanb	B1	vcanb_B1_5	TCACAGCTGCGTTGACTTGATCCTCTAGAAGAGTCTTCCTTTACG
vcanb	B1	vcanb_B1_6	GAGGAGGGCAGCAAACGGAATTCTACTATATACATTTAAGCCCCG
vcanb	B1	vcanb_B1_7	TTCTGCTGTTTTTGACCAGCGATGGTAGAAGAGTCTTCCTTTACG
vcanb	B1	vcanb_B1_8	GAGGAGGGCAGCAAACGGAAGTACTGAGATTCACTGAAGCGTCTC
vcanb	B1	vcanb_B1_9	CAGGACACTGTGCCCTTCTTACAGGTAGAAGAGTCTTCCTTTACG
vcanb	B1	vcanb_B1_10	GAGGAGGGCAGCAAACGGAAAAGGTCAGGTGGTAGTTGCAGGGCA
vcanb	B1	vcanb_B1_11	GACGACACTCTCTTTCTGCTGCCTCTAGAAGAGTCTTCCTTTACG
vcanb	B1	vcanb_B1_12	GAGGAGGGCAGCAAACGGAAACGTCCGCCGGTGGGTGAAGTACTT
vcanb	B1	vcanb_B1_13	GCCGTTTTCACACACACTGACCGAGTAGAAGAGTCTTCCTTTACG
vcanb	B1	vcanb_B1_14	GAGGAGGGCAGCAAACGGAAAAGTGCGTGATCTTGCAAATCCACC
vcanb	B1	vcanb_B1_15	GCAATAGTGATGGGGCCACTGGAATTAGAAGAGTCTTCCTTTACG
vcanb	B1	vcanb_B1_16	GAGGAGGGCAGCAAACGGAAACAGACGTTGAGATGAGAGGCTCCT
vcanb	B1	vcanb_B1_17	CAAATGCTTTAGTTGGTTCATTTGCTAGAAGAGTCTTCCTTTACG
vcanb	B1	vcanb_B1_18	GAGGAGGGCAGCAAACGGAACAACACTAGTTTCAACAGTTTGTTG
vcanb	B1	vcanb_B1_19	ACTAGCAGGTTCCCTTGGGTCTTTGTAGAAGAGTCTTCCTTTACG
vcanb	B1	vcanb_B1_20	GAGGAGGGCAGCAAACGGAAATGAGTACTTGTTGAGGAAGTTGTA
vcanb	B1	vcanb_B1_21	CCACCTATTTCAGTCTCGTCGGTAGTAGAAGAGTCTTCCTTTACG
vcanb	B1	vcanb_B1_22	GAGGAGGGCAGCAAACGGAAACCATATCTGGGTCAGTAGAAGCTG
vcanb	B1	vcanb_B1_23	CAGTTTTGTAGGAAGATGTAAGACCTAGAAGAGTCTTCCTTTACG
vcanb	B1	vcanb_B1_24	GAGGAGGGCAGCAAACGGAACAGCTTCGGCCAGAACTATTACTAT
vcanb	B1	vcanb_B1_25	TTCATCTGTTTTAGGGGAAGATACATAGAAGAGTCTTCCTTTACG
vcanb	B1	vcanb_B1_26	GAGGAGGGCAGCAAACGGAAACCTTCAAATTCTGACATAAGAATT
vcanb	B1	vcanb_B1_27	AAATCCAGAACACTTTCAACTGATTTAGAAGAGTCTTCCTTTACG
vcanb	B1	vcanb_B1_28	GAGGAGGGCAGCAAACGGAATTTGTATCCTTGATGTCGACTATGA
vcanb	B1	vcanb_B1_29	CGCTGATGCTTCCCTCAGCACTACTTAGAAGAGTCTTCCTTTACG
vcanb	B1	vcanb_B1_30	GAGGAGGGCAGCAAACGGAAATTCCCCATGAGGTGTATCCAAAGG
vcanb	B1	vcanb_B1_31	TGGTGCCATGCTTGCAGAGAACATTTAGAAGAGTCTTCCTTTACG
vcanb	B1	vcanb_B1_32	GAGGAGGGCAGCAAACGGAAAGGTGGTTCTTCTATGGTGTCATCG
vcanb	B1	vcanb_B1_33	CCGTCCGACAACCAGCCGAAATCGCTAGAAGAGTCTTCCTTTACG

vcanb	B1	vcanb_B1_34	GAGGAGGGCAGCAAACGGAATGGTCCATGCCGTCTCTCCAGGCGG
vcanb	B1	vcanb_B1_35	CGGCCATCCATCCGGCGTCACACTGTAGAAGAGTCTTCCTTTACG
vcanb	B1	vcanb_B1_36	GAGGAGGGCAGCAAACGGAACGAATCCGTCCTCGTATGCTGAATA
vcanb	B1	vcanb_B1_37	GCTGGGCACTGACACCCGGCCCATATAGAAGAGTCTTCCTTTACG
vcanb	B1	vcanb_B1_38	GAGGAGGGCAGCAAACGGAACTCTTGGCCCATTTTGACGATGCCG
vcanb	B1	vcanb_B1_39	ATGTGCTTCACGTCCAACAACATCATAGAAGAGTCTTCCTTTACG
vcanb	B1	vcanb_B1_40	GAGGAGGGCAGCAAACGGAATCAAACTTATTTTTCCAGTTCCTGA
gpr126	B4	gpr126_B4_1	TCTGAATGTCCAGACGCAATACAGAATTCTCACCATATTCGCTTC
gpr126	B4	gpr126_B4_2	CCTCAACCTACCTCCAACAACTTCATTAGGAAATTATCTTACTGT
gpr126	B4	gpr126_B4_3	ATATGAAGGTCTGAATGTGTTAGATATTCTCACCATATTCGCTTC
gpr126	B4	gpr126_B4_4	CCTCAACCTACCTCCAACAAGGTGTATAGCTGTTGCTTTCCGTTT
gpr126	B4	gpr126_B4_5	GGGAAAAATGCAAGCTCCCAACCATATTCTCACCATATTCGCTTC
gpr126	B4	gpr126_B4_6	CCTCAACCTACCTCCAACAATTGTTCTTTGAGCCCCCAACAGAGG
gpr126	B4	gpr126_B4_7	ATATTTACAGATCACATAGTCAGTAATTCTCACCATATTCGCTTC
gpr126	B4	gpr126_B4_8	CCTCAACCTACCTCCAACAAAGCTGAAAATCACAGTTTGTAAAAT
gpr126	B4	gpr126_B4_9	GACCTGGTGCACAGGAAGAATGGAGATTCTCACCATATTCGCTTC
gpr126	B4	gpr126_B4_10	CCTCAACCTACCTCCAACAAGGAAGGCTCTCCGTCAGAAGGGCTG
gpr126	B4	gpr126_B4_11	TTAGTGGCAGTCTTGCTCCAGTCTGATTCTCACCATATTCGCTTC
gpr126	B4	gpr126_B4_12	CCTCAACCTACCTCCAACAATTATCTGCCAAGCGTAACTTTCCAC
gpr126	B4	gpr126_B4_13	TATCCTCTCGCAGTGTCCGGTTGCTATTCTCACCATATTCGCTTC
gpr126	B4	gpr126_B4_14	CCTCAACCTACCTCCAACAAGCTTGCCGTTACGTCCACAGATTTG
gpr126	B4	gpr126_B4_15	CCATCCCACGATGCAAAACTTGAGGATTCTCACCATATTCGCTTC
gpr126	B4	gpr126_B4_16	CCTCAACCTACCTCCAACAAGTATCTCCGAATGTATGTGTTGAAG
gpr126	B4	gpr126_B4_17	CGCCGCAGCTTCTCAAAAGCGATGTATTCTCACCATATTCGCTTC
gpr126	B4	gpr126_B4_18	CCTCAACCTACCTCCAACAAGTGAGCAGTGTTGCCGCTGAAAAAA
gpr126	B4	gpr126_B4_19	TGAAATCCCAAAACACACACTGAGGATTCTCACCATATTCGCTTC
gpr126	B4	gpr126_B4_20	CCTCAACCTACCTCCAACAATCGGATCTTTCTGATACTCCAAATG
gpr126	B4	gpr126_B4_21	GACCACAGCCAATGCATTATGTGCCATTCTCACCATATTCGCTTC
gpr126	B4	gpr126_B4_22	CCTCAACCTACCTCCAACAACGAGTCAAAATCAATCTGAGGGTCT
gpr126	B4	gpr126_B4_23	GAAATGATGGTGACCACAGTGCTGGATTCTCACCATATTCGCTTC
gpr126	B4	gpr126_B4_24	CCTCAACCTACCTCCAACAAAGGGTGGCGTTGATTTTGGCTATGT
gpr126	B4	gpr126_B4_25	CGTTTCGATCTTTGTAAGGGAAACAATTCTCACCATATTCGCTTC
gpr126	B4	gpr126_B4_26	CCTCAACCTACCTCCAACAAGGACATACTGAGTGACTGTGGGTCT
gpr126	B4	gpr126_B4_27	CCTTGAGAGAACAGTGATAAGCTGAATTCTCACCATATTCGCTTC
gpr126	B4	gpr126_B4_28	CCTCAACCTACCTCCAACAAACTGATGCCATCAACATAAACTCTA
gpr126	B4	gpr126_B4_29	CAACCTGCGGTTCCTGGTGAAAGAGATTCTCACCATATTCGCTTC
gpr126	B4	gpr126_B4_30	CCTCAACCTACCTCCAACAAGTTATGGCAGTACTGCAGCTGAGCG
gpr126	B4	gpr126_B4_31	ATCCGCCACTCTGCAGTGTGTAAATATTCTCACCATATTCGCTTC
gpr126	B4	gpr126_B4_32	CCTCAACCTACCTCCAACAAGAGAGGCCGAGCAGATGCTGGAGAA

gpr126	B4	gpr126_B4_33	GGTCTCTGTGGCCTTCTGTGCAGTGATTCTCACCATATTCGCTTC
gpr126	B4	gpr126_B4_34	CCTCAACCTACCTCCAACAAGGCGATCTCAAAGCACACCGTGAAG
gpr126	B4	gpr126_B4_35	AAGCCGCAAAATTTGGCATCGCTGGATTCTCACCATATTCGCTTC
gpr126	B4	gpr126_B4_36	CCTCAACCTACCTCCAACAACCGGTCTTGACGACAACGCGGTCAT
gpr126	B4	gpr126_B4_37	AAAGGCAGATCAGCAGCAGGAAAACATTCTCACCATATTCGCTTC
gpr126	B4	gpr126_B4_38	CCTCAACCTACCTCCAACAACAAGAGTATTCTGGAACTTCCATCT
gpr126	B4	gpr126_B4_39	TAAATGTCGGTTTTTTGACAGATGAATTCTCACCATATTCGCTTC
gpr126	B4	gpr126_B4_40	CCTCAACCTACCTCCAACAACTGCGCTCCAGGCAGACAGATGCTG
col2a1a	B4	col2a1a_B4_1	GATGACATCAAGCCATGTTTCTGTCATTCTCACCATATTCGCTTC
col2a1a	B4	col2a1a_B4_2	CCTCAACCTACCTCCAACAATCATTGGTAGTGCTTGCATGTTCGG
col2a1a	B4	col2a1a_B4_3	AGTGTTTTGCATCCTCACAGTTATTATTCTCACCATATTCGCTTC
col2a1a	B4	col2a1a_B4_4	CCTCAACCTACCTCCAACAATCGTCATTGGTATTTTTCCATGTCT
col2a1a	B4	col2a1a_B4_5	GTACGCCATATGTAAAGCGGCTGTTATTCTCACCATATTCGCTTC
col2a1a	B4	col2a1a_B4_6	CCTCAACCTACCTCCAACAACCTCTGCTCTGATCTCCACATCATT
col2a1a	B4	col2a1a_B4_7	GAACCACACGTGCTTCTGGGCCTTGATTCTCACCATATTCGCTTC
col2a1a	B4	col2a1a_B4_8	CCTCAACCTACCTCCAACAACTTGCTTGTCCACCAGTTCTTGCGT
col2a1a	B4	col2a1a_B4_9	TGCCCGTTGATGGACTTCAGAGTGGATTCTCACCATATTCGCTTC
col2a1a	B4	col2a1a_B4_10	CCTCAACCTACCTCCAACAATCCACCTCTACATCGTGTTGTCTGA
col2a1a	B4	col2a1a_B4_11	GCTGACCATTAGAACCATCCTTACCATTCTCACCATATTCGCTTC
col2a1a	B4	col2a1a_B4_12	CCTCAACCTACCTCCAACAACAGGTCCAACAGGTCCTGAAGGTCC
col2a1a	B4	col2a1a_B4_13	AGGTCCTTGTGGGCCATTCTCTCCTATTCTCACCATATTCGCTTC
col2a1a	B4	col2a1a_B4_14	CCTCAACCTACCTCCAACAAGTCTCCCTGTTTGCCAATTGGACCA
col2a1a	B4	col2a1a_B4_15	CCTCCTGGAGCTCCCTGTTTGCCAGATTCTCACCATATTCGCTTC
col2a1a	B4	col2a1a_B4_16	CCTCAACCTACCTCCAACAATCACCAGAAGGTCCTGGAAGTCCAG
col2a1a	B4	col2a1a_B4_17	GACCATCCTTACCAGAAGGACCTGCATTCTCACCATATTCGCTTC
col2a1a	B4	col2a1a_B4_18	CCTCAACCTACCTCCAACAAGGCCGGCAGCACCAGGGTTACCGTT
col2a1a	B4	col2a1a_B4_19	GCCATCAGCACCAGGGGGTCCAGCAATTCTCACCATATTCGCTTC
col2a1a	B4	col2a1a_B4_20	CCTCAACCTACCTCCAACAAGCCAGCAGGTCCAGGTGCACCAATC
col2a1a	B4	col2a1a_B4_21	CCAACAGCTCCTCTCTCACCAGGCAATTCTCACCATATTCGCTTC
col2a1a	B4	col2a1a_B4_22	CCTCAACCTACCTCCAACAACCTTGAAGACCGGGAGGACCTTGAG
col2a1a	B4	col2a1a_B4_23	CGGGGGCTCCAGTAGGTCCAGGCAGATTCTCACCATATTCGCTTC
col2a1a	B4	col2a1a_B4_24	CCTCAACCTACCTCCAACAACCTGGAAGCCAGATGGACCAGGTTG
col2a1a	B4	col2a1a_B4_25	AGGTGGTCCAGGGCGGCCATCTTCAATTCTCACCATATTCGCTTC
col2a1a	B4	col2a1a_B4_26	CCTCAACCTACCTCCAACAAAGGGGCACCAGTCGCTCCAACTTTT
col2a1a	B4	col2a1a_B4_27	GGAGGTCCAAGAGGTCCGGCAGAACATTCTCACCATATTCGCTTC
col2a1a	B4	col2a1a_B4_28	CCTCAACCTACCTCCAACAAGGCTCTCCTCTTGGTCCTCTCTTGC
col2a1a	B4	col2a1a_B4_29	CAGATCCTTTAGCTCCAGGAATACCATTCTCACCATATTCGCTTC
col2a1a	B4	col2a1a_B4_30	CCTCAACCTACCTCCAACAACAGTACCAGGGTTACCGGATGCACC
col2a1a	B4	col2a1a_B4_31	TGCACCAGGGCGACCTCTCTCACCGATTCTCACCATATTCGCTTC

col2a1a	B4	col2a1a_B4_32	CCTCAACCTACCTCCAACAACAGACCACGAGGACCCATTGGTCCA
col2a1a	B4	col2a1a_B4_33	CTTCCGGGTTTTCCAGGGGGGCCGGATTCTCACCATATTCGCTTC
col2a1a	B4	col2a1a_B4_34	CCTCAACCTACCTCCAACAAGGGCCACGGGGTCCAAGGGCACCAG
col2a1a	B4	col2a1a_B4_35	GTCCGGGTGGTCCAGGGGGTCCTGGATTCTCACCATATTCGCTTC
col2a1a	B4	col2a1a_B4_36	CCTCAACCTACCTCCAACAATTCCAGGTGTACCAGGCTCGCCATC
col2a1a	B4	col2a1a_B4_37	CTCTCCAGGTGAAATGATGGGATTGATTCTCACCATATTCGCTTC
col2a1a	B4	col2a1a_B4_38	CCTCAACCTACCTCCAACAAACAGTCATTCAGATCCTCACAGATG
col2a1a	B4	col2a1a_B4_39	AATCTGAACATGTCTAAAGATTAGAATTCTCACCATATTCGCTTC
col2a1a	B4	col2a1a_B4_40	CCTCAACCTACCTCCAACAATGCAGGTCCTAAGGGGTGAAAGTCG
col2a1a	B2	col2a1a_B2_1	GATGACATCAAGCCATGTTTCTGTCAAATCATCCAGTAAACCGCC
col2a1a	B2	col2a1a_B2_2	CCTCGTAAATCCTCATCAAATCATTGGTAGTGCTTGCATGTTCGG
col2a1a	B2	col2a1a_B2_3	AGTGTTTTGCATCCTCACAGTTATTAAATCATCCAGTAAACCGCC
col2a1a	B2	col2a1a_B2_4	CCTCGTAAATCCTCATCAAATCGTCATTGGTATTTTTCCATGTCT
col2a1a	B2	col2a1a_B2_5	GTACGCCATATGTAAAGCGGCTGTTAAATCATCCAGTAAACCGCC
col2a1a	B2	col2a1a_B2_6	CCTCGTAAATCCTCATCAAACCTCTGCTCTGATCTCCACATCATT
col2a1a	B2	col2a1a_B2_7	GAACCACACGTGCTTCTGGGCCTTGAAATCATCCAGTAAACCGCC
col2a1a	B2	col2a1a_B2_8	CCTCGTAAATCCTCATCAAACTTGCTTGTCCACCAGTTCTTGCGT
col2a1a	B2	col2a1a_B2_9	TGCCCGTTGATGGACTTCAGAGTGGAAATCATCCAGTAAACCGCC
col2a1a	B2	col2a1a_B2_10	CCTCGTAAATCCTCATCAAATCCACCTCTACATCGTGTTGTCTGA
col2a1a	B2	col2a1a_B2_11	GCTGACCATTAGAACCATCCTTACCAAATCATCCAGTAAACCGCC
col2a1a	B2	col2a1a_B2_12	CCTCGTAAATCCTCATCAAACAGGTCCAACAGGTCCTGAAGGTCC
col2a1a	B2	col2a1a_B2_13	AGGTCCTTGTGGGCCATTCTCTCCTAAATCATCCAGTAAACCGCC
col2a1a	B2	col2a1a_B2_14	CCTCGTAAATCCTCATCAAAGTCTCCCTGTTTGCCAATTGGACCA
col2a1a	B2	col2a1a_B2_15	CCTCCTGGAGCTCCCTGTTTGCCAGAAATCATCCAGTAAACCGCC
col2a1a	B2	col2a1a_B2_16	CCTCGTAAATCCTCATCAAATCACCAGAAGGTCCTGGAAGTCCAG
col2a1a	B2	col2a1a_B2_17	GACCATCCTTACCAGAAGGACCTGCAAATCATCCAGTAAACCGCC
col2a1a	B2	col2a1a_B2_18	CCTCGTAAATCCTCATCAAAGGCCGGCAGCACCAGGGTTACCGTT
col2a1a	B2	col2a1a_B2_19	GCCATCAGCACCAGGGGGTCCAGCAAAATCATCCAGTAAACCGCC
col2a1a	B2	col2a1a_B2_20	CCTCGTAAATCCTCATCAAAGCCAGCAGGTCCAGGTGCACCAATC
col2a1a	B2	col2a1a_B2_21	CCAACAGCTCCTCTCTCACCAGGCAAAATCATCCAGTAAACCGCC
col2a1a	B2	col2a1a_B2_22	CCTCGTAAATCCTCATCAAACCTTGAAGACCGGGAGGACCTTGAG
col2a1a	B2	col2a1a_B2_23	CGGGGGCTCCAGTAGGTCCAGGCAGAAATCATCCAGTAAACCGCC
col2a1a	B2	col2a1a_B2_24	CCTCGTAAATCCTCATCAAACCTGGAAGCCAGATGGACCAGGTTG
col2a1a	B2	col2a1a_B2_25	AGGTGGTCCAGGGCGGCCATCTTCAAAATCATCCAGTAAACCGCC
col2a1a	B2	col2a1a_B2_26	CCTCGTAAATCCTCATCAAAAGGGGCACCAGTCGCTCCAACTTTT
col2a1a	B2	col2a1a_B2_27	GGAGGTCCAAGAGGTCCGGCAGAACAAATCATCCAGTAAACCGCC
col2a1a	B2	col2a1a_B2_28	CCTCGTAAATCCTCATCAAAGGCTCTCCTCTTGGTCCTCTCTTGC
col2a1a	B2	col2a1a_B2_29	CAGATCCTTTAGCTCCAGGAATACCAAATCATCCAGTAAACCGCC
col2a1a	B2	col2a1a_B2_30	CCTCGTAAATCCTCATCAAACAGTACCAGGGTTACCGGATGCACC

col2a1a	B2	col2a1a_B2_31	TGCACCAGGGCGACCTCTCTCACCGAAATCATCCAGTAAACCGCC
col2a1a	B2	col2a1a_B2_32	CCTCGTAAATCCTCATCAAACAGACCACGAGGACCCATTGGTCCA
col2a1a	B2	col2a1a_B2_33	CTTCCGGGTTTTCCAGGGGGGCCGGAAATCATCCAGTAAACCGCC
col2a1a	B2	col2a1a_B2_34	CCTCGTAAATCCTCATCAAAGGGCCACGGGGTCCAAGGGCACCAG
col2a1a	B2	col2a1a_B2_35	GTCCGGGTGGTCCAGGGGGTCCTGGAAATCATCCAGTAAACCGCC
col2a1a	B2	col2a1a_B2_36	CCTCGTAAATCCTCATCAAATTCCAGGTGTACCAGGCTCGCCATC
col2a1a	B2	col2a1a_B2_37	CTCTCCAGGTGAAATGATGGGATTGAAATCATCCAGTAAACCGCC
col2a1a	B2	col2a1a_B2_38	CCTCGTAAATCCTCATCAAAACAGTCATTCAGATCCTCACAGATG
col2a1a	B2	col2a1a_B2_39	AATCTGAACATGTCTAAAGATTAGAAAATCATCCAGTAAACCGCC
col2a1a	B2	col2a1a_B2_40	CCTCGTAAATCCTCATCAAATGCAGGTCCTAAGGGGTGAAAGTCG

Extended Table 2

Species	Protein	Domain	Amino Acid sequence
Homo sapiese	CCN1	IGFBP	STCPAACHCPLEAPKCAPGVGLVRDGCGCCKVCAKQLNEDCSKTQPCDHTKGLECNFGASSTALKGICRA
Homo sapiens	CCN1	VWC	CEYNSRIYQNGESFQPNCKHQCTCIDGAVGCIPLCPQELSLPNLGCPNPRLVKVTGQCCEEWVC
Homo sapiens	CCN1	TSP-1	-VQTTSWSQCSKTCGTGISTRVTNDNPECRLVKETRICEVRPCG
Homo sapiens	CCN1	CT	KSPEPVRFTYAGCLSVKKYRPKYCGSCVDGRCCTPQLTRTVKMRFRCEDGE--TFSKNVMMIQSCKCNYNCP
Danio rerio	Ccn1	IGFBP	SSCPAVCSCAPDAPQCPPGVGLQRDACGCCLVCARQLNEDCSRSEPCDHSKGLECNYGASHGATRGICR-
Danio rerio	Ccn1	VWC	CEYSSRIYQNGESFQPNCKHQCTCMDGAVGCVPLCPQELSLPALGCANPRLVKVPGRCCEEWVC
Danio rerio	Ccn1	TSP-1	-VQTTGWSQCSRSCGTGISTRITNNNAECKLMKESRICEVRPCS
Danio rerio	Ccn1	CT	KSVTPVKFSYAGCSSLKKYRPRFCGSCVDGRCCSPQNTRTIRVKFRCQDGE--TFNKNVMMIESCKCTKHCP-
Danio rerio	Ccn1l1	IGFBP	GCPLKCSCPSAPPSCPPGISSVLDHCGCCRVCARQFNQDCGSPTEPCDHIKGLRCHLGAEGDPDRGLCRA
Danio rerio	Ccn1l1	VWC	CELDGRIYQHGEDFQPSCEHQCTCVDGVVGCLPLCPHHISLPDWRCARRRLIRKPERCCPEWVC
Danio rerio	Ccn1l1	TSP-1	LLQITDWSPCSATCGMGVSSRVTNSNPECRLVSETRLCQIRECG
Danio rerio	Ccn1l1	CT	RPQKPVQISFAGCSTTRRYRLRSCGFCSDGRLCVPSATRTVRLHFHCPEAERHDFTRSLMWIQRCSCRHTHSR